공학박사 학위논문

First-principles study on the role of interface and defect on instability of amorphous semiconducting oxide

비정질 산화물 반도체의 신뢰성에 계면과 결함이 미치는 역할에 대한 제일원리 연구

2019년 2월

서울대학교 대학원

재료공학부

송호철

Abstract

First-principles study on the role of interface and defect on instability of amorphous semiconducting oxide

Hochul Song

Department of Materials Science and Engineering

The Graduate School

Seoul National University

Amorphous oxide semiconductors (AOSs) are currently recognized as key materials for thin-film transistor (TFT) in next-generation flat panel displays because AOS-based TFTs exhibit high field-effect mobility. Despite many advantages, AOSs-based TFT has critical issues related to the instability induced by illumination stress. Among various types of defects, oxygen vacancy (V_O) and the interface between AOS and gate insulator have been the suspect of being origin of the instabilities.

The electronic structure of V_O in AOSs was explored using first-principles calculations in earlier works. However, different groups drew a contradictive conclusion on the nature of V_O (shallow vs.

deep). In addition, computational approaches used in previous studies would cause some ambiguities in interpretation of calculation results hindering definite conclusions; (1) energetics of V_O were usually studied using semi-local functionals, which tends to favor the shallow defect via lowering the energy cost to add an electron to conduction band due to the band gap underestimation. (2) A method to generate V_O, namely removal of one oxygen atom in constructed amorphous supercells, would not reflect the actual relaxation process of neighboring atoms in amorphous phase where the V_O site is ill-defined. Therefore, despite many theoretical investigations, the nature of V_O in AOSs is still controversial. In this work, we explore the electronic structure and energetics of V_O in amorphous $InGaZnO_4$ (a-IGZO) which is one of the representative AOSs using density functional theory (DFT) calculations. Here we employ a distinct approach from previous works: hybrid density functional molecular dynamics calculations, which allows us to avoid any ambiguity in interpretation of calculation results mentioned above. We examine eight individual amorphous structures with V_O. Without any exception, we find the Fermi level to be located around the conduction band minimum, implying that the majority of V_O is shallow donor in AOSs. We further confirm this conclusion by comparing energies between shallow and deep V_O. To this end, we create five amorphous structures including deep V_O using the same calculation setups, but adding extra electrons in the supercell during MD simulations, and then, final energies of deep V_O are obtained by removing extra electrons. We show that the shallow V_O is lower in energy on

average than deep V_O, supporting that V_O is likely to be shallow in AOSs. Our results are indeed consistent with experiments that oxygen-poor environment leads to the higher carrier concentration.

In addition, many previous studies report the significant negative shift of the threshhold voltage in TFTs under the negative-bias-illumination stress (NBIS) conditions and hole trap at the interface between AOS and gate insulator is suspected to be a major origin of the threshold shift. In this research, we modeled the atomic structure of the interface between a-IGZO and a-SiO_2 using the first-principles MD simulation. We perform MD simulations through various modeling protocols to find out energetically favorable structure of amorphous/amorphous interface structure. We evaluate the band offset between a-IGZO and a-SiO_2 from the interface model and the result shows good agreement with experimental value. In addition, we study on the oxygen-deficient conditions as well, which reveals that the metal silicate bonding leads to hole-trapping sites at the interface.

Keywords: density functional theory, amorphous semiconducting oxides, oxygen vacancy, amorphous interface, hole trap site
Student Number: 2014-30224

Contents

Abstract ·····

Contents ·····

1. Introduction ·····1

1.1. Overview of amorphous semiconducting oxide ·····1

1.2. Instability issues in amorphous semiconducting oxide ·5

1.3. Overview of V_O researches on amorphous semiconducting oxide 9

1.4. Goal of the dissertation ·····18

2. Theoretical background ·····20

2.1. First-principles calculation : density functional theory (DFT) 20

2.1.1. Hohenberg and Kohn theorem ·····20

2.1.2. Kohn-Sham equation ·····23

2.1.3. Exchange-correlation energy ·····25

2.2. Beyond DFT ·····27

2.2.1. DFT+U ·····27

2.1.2. Hybrid functional ·····28

2.3. Inverse Participation Ratio (IPR) ·····30

2.4. Defect formation energy ·····31

3. Nature of V_O in amorphous oxide semiconductors ···32

3.1. Introduction ·····32

3.2. Calculation method ·····34

3.2.1. Band gap correction ·····34

3.2.2. Band filling correction ·····37

3.2.3. Oxygen deficient melt-quench protocol ·····40

3.2.3.1 Problem of post-removal scheme ·····41

3.2.4. Computation details ·····44

3.3. Results and discussion ·····47

3.3.1 Shallow V_O ·····47

3.3.1.1 Atomic structural ·····47

3.3.1.2 Electronic structure ·····51

3.3.2 Deep V_O ·····55

3.3.3 Comparison between shallow and deep V_O ·····60

3.3.4 Role of V_O in a-IGZO ·····63

4. Modeling of the a-IGZO/a-SiO2 interfaces ·····64

4.1. Computational details ·····64

4.2. Generating interface structures ·····66

4.3. Exchange-correlation functional dependance ·····71

4.4. Character of interface structures ·····79

4.5. Localized states in amorphous structures ·····82

4.6. Band alignment ·····85

4.7. Partial density of states ·····90

4.8. V_O at the interface ·····95

5. Conclusion ·····100

Bibliography ·····102

국문초록 ·····108

List of table and figures

Table 3.1. Averaged values of the bond length (r) between metal and oxygen ions and coordination numbers (Nc) around metal ions in a-$IGZO_{4-x}$. The values in the parenthesis are for a-$IGZO_4$. ····· 50

Table 4.1. Energy difference between different methods of constructing interfaces. ····· 69

Table 4.2. Local structural parameters for a-$IGZO_4$ with different functional ····· 75

Table 4.3. Local structural parameters for a-SiO_2 with different functional ····· 77

Table 4.4. Difference of the average bond length in bulk and interface ····· 81

Figure 1.1. TFTs using AOS as the channel layer ····· 2

Figure 1.2. (a) Device structure of TFT. a-IGZO channel layer deposited on a plastic substrate. (b) Hall mobility of amorphous and crystalline IGZO films. ····· 4

Figure 1.3. (a) Persistent photoconductivity in IGZO. (b) and (c) show transfer characteristics with positive and negative shift of the threshold voltage under positive and negative bias stress, respectively. (d) The variation of transfer curve under 410 nm light illumination with -20 V gate bias. ····· 7

Figure 1.4. Interface hole traps that made of V_O ····· 8

Figure 1.5. Norms of HOMO wave functions (yellow surfaces show iso-surfaces and blue areas show their cross-sections) for oxygen deficient a-IGZO obtained by LDA calculations. (a)Model 1, and (b) model 2. Purple, green, grey and red spheres represent In, Ga, Zn

and O ions, respectively. ····· 11

Figure 1.6. Calculated DOSs of oxygen deficient a-IGZO. (a) Model 1, and (b) Model 2. The energy is measured from the VBM. ····· 12

Figure 1.7. Isosurfaces of the charge densities for the deep levels of V_O, with the (a)In or (b) Ga atoms in the neighborhood, and (c) the shallow V_O defect surrounded by one Ga and three Zn atoms, with electrons in the CBM. ····· 13

Figure 1.8. Schematic illustrations of the photoexcitation of electron-hole pairs and the V_O defects, the drift motion of hole carriers, the hole trapping in the channel/dielectric interface (a)under the NBIS and (b) after switching off the NBIS. In (b), a potential well is developed due to the band bending at the interface. ····· 15

Figure 1.9. Distribution of the signature of the localized Kohn-sham states for 60 different models of an oxygen deficient a-IGZO and for five different charge states. The figure represents the position in energy (at gamma) of the Kohn-Sham states of the conduction band (blue), valence band (green), and of the states in the bandgap due to the localized Metal-Metal state (red) when they are present. ····· 16

Figure 1.10. The average formation energies of V_O defects with Ga-Ga, Ga-M, and M-M bonds [V_O(Ga-Ga), V_OGa-M),and V_O(M-M), respectively] as functions of the Fermi energy for the neutral and +2 charge states. ····· 17

Figure 3.1. Band structures of a-$IGZO_{4-x}$ models in (a) GGA+U, (b) HSE06 ····· 36

Figure 3.2. The schematic band structure of the deep and shallow V_O^0 states. The dashed lines represent the special k points used in the supercell calculations. The energy position of $E_{CBM,k-av}$, $E_{CBM,\Gamma}$,

$E_{D,k-av}$, and $E_{D,\Gamma}$ are also indicated. ····· 39

Figure 3.3. Schematic diagram of different configuration space between stoichiometric and oxygen deficient structures. ····· 42

Figure 3.4. Schematic diagram of oxygen deficient melt-quench protocol. The sample in which an oxygen is removed is annealed at high temperature in long time. Then some images of the MD simulation is chosen to be quenched. ····· 46

Figure 3.5. (a) Ion-averaged pair distribution functions for metal-oxygen (M-O) and metal-metal (M-M) pairs in a-$IGZO_{4-x}$ and a-$IGZO_4$. (b) Cavities in an a-$IGZO_{4-x}$ model identified by the Connolly analysis. ····· 49

Figure 3.6. (a) Calculated band structure and IPR for a deep V_O model. The arrow indicates the deep state associated with V_O and its IPR values are marked in dashed ellipsoid. Isosurface in (b) is the distribution of the charge density of the deep level. ····· 53

Figure 3.7. Schematic diagram of change after 2 extra electron added melt-quench process. (a) is a normal oxygen deficient a-$IGZO_4$ model and green line denotes the level which 2 extra electron would occupy. During melt-quench process, a-$IGZO_{4-x}$ would change atomic structure to reduce the energy of 2 extra electron. In the result, a deep level defect is made. ····· 57

Figure 3.8. (a) Calculated band structure and IPR for a deep V_O model. The arrow indicates the deep state associated with V_O and its IPR values are marked in dashed ellipsoid. Isosurface in (b) is the distribution of the charge density of the deep level. ····· 58

Figure 3.9. Cavities in an deep a-$IGZO_{4-x}$ model identified by the Connolly analysis. ····· 59

Figure 3.10. (a) Formation energy of deep and shallow oxygen

vacancies. The shaded area represents the distribution of oxygen vacancy formation energy obtained by applying Gaussian broadening with a standard deviation of 0.4 eV. (b) Schematic energy-configuration diagram for oxygen vacancies in a-IGZO. ···· 62

Figure 4.1. Temperature protocol of melt-quench method of making each of amorphous structures ····· 67

Figure 4.2. Volume dependance on exchange-correlation functional in crystal structure of In_2O_3, Ga_2O_3, ZnO, SiO_2. ····· 73

Figure 4.3. Radial distribution function of *a*-$IGZO_4$ calculated by PBEsol functional. ····· 74

Figure 4.4. Radial distribution function of *a*-SiO_2 calculated by PBEsol functional. ····· 76

Figure 4.5. Interface model constructed by slice-and-connect method. ····· 80

Figure 4.6. Inverse-participation ratios value of *a*-$IGZO_4$ and *a*-SiO_2, respectively. ····· 84

Figure 4.7. Oxygen 2*s* level chosen as reference level (red dots), and averaged line (blue line). ····· 87

Figure 4.8. Band offset calculated from GGA of interface between *a*-SiO2/*a*-IGZO. Gray lines represent locaized tail state edges. ····· 89

Figure 4.9. Partial DOS of *a*-$IGZO_4$-bulk-like region, interface region and *a*-SiO_2 bulk-like region ····· 92

Figure 4.10. The schematic diagram for the electronic structure of the constructed interface is shown. The calculated first-moment peaks for oxygen 2s level are plotted. The plateaus in the macroscopic average indicate the bulk regions of a-SiO_2 and a-$IGZO_4$. ····· 93

Figure 4.11. Calculated partial density of states that is spatially resolved along the z-direction. ····· 94
Figure 4.12. The formation energy of the neutral oxygen vacancy is shown with respect to the z-coordination. The vacancies are classified into four types according to neighboring cations. ····· 97
Figure 4.12. The local densities of states and atomic structures of (a) deep V_O[M-Si] and (b) resonant V_O[M···Si] are shown. The isosurface of the charge density of the defect state marked by the dashed circle in (a) is shown in the right. The isovalue is 3.4×10^{-3} e $Å^{-3}$ ····· 99

CHAPTER 1

Introduction

1.1. Overview of amorphous semiconducting oxide

Amorphous oxide semiconductors (AOSs), which are represented by amorphous $InGaZnO_4$ (*a*-IGZO), are promising materials to be used as channel layers of thin-film transistors (TFTs) in next-generation displays, because they have excellent electrical properties [ref]. Compared with other materials used as channel layers of TFTs in displays, AOSs have many advantages such as (i) the good uniformity of the amorphous structure to fabricate large area display devices and (ii) high electron mobility ($\geq$ 10 $cm^2/V \cdot s$) to produce high performance TFT devices. [1]

In 2003, Nomura et al. [2] announced successful fabrication of the TFTs using the single crystalline $InGaO_3(ZnO)_5$ (sc-$IGZO_5$) active layer, which made the development of AOS-based TFTs prominent. Prior to the announcement of Nomura, there have been several attempts to develop TFT using AOSs, but the performance of TFT was not hopeful because it was difficult to handle the carrier concentration of the oxides such as ZnO and In_2O_3 which are used as conducting materials. [3,4] In addition, AOSs film has many grain-boundaries, which

substantially suppress the carrier mobility because of grain-boundary scattering. For example, it was reported that ZnO TFTs exhibited unacceptable performance with ~10^3 on-off ratio showing normally-on

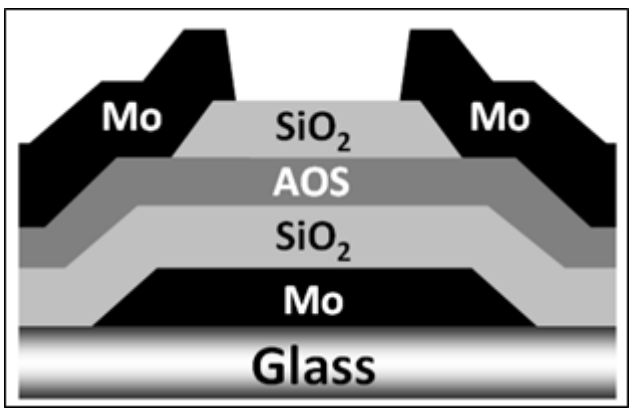

Figure 1.1. TFTs using AOS as the channel layer

characteristics or low field-effect mobility of ~3 cm^2/Vs due to many grain-boundaries in a normally-off device. [5-7] It was demonstrated that, however, the single crystalline phase of $IGZO_5$ was well deposited on the substrate and its TFT characteristics showed outstanding performance with an on-off current ratio of ~10^6 and ~80 $cm^{2/}$Vs of field-effect mobility in the on state.

More interestingly, TFT using amorphous In-Ga-Zn-O (a-IGZO) was developed in 2004. [1] The TFT with a-IGZO channel layer which was

deposited on a plastic substrate showed excellent performances displaying the comparable electron mobility with that of its crystalline counterpart even though it was fabricated at room temperature without additional annealing process as shown in Fig 1.2. [1] Because it has been difficult to produce high-performance device using low-temperature fabrication method due to a trade-off relation between fabrication temperature and device performance, the appearance of a-IGZO has attracted tremendous interests triggering the intensive researches on AOSs.

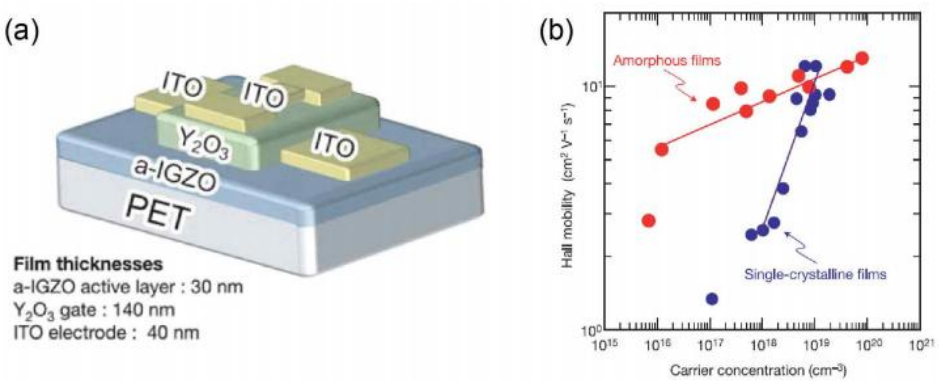

Figure 1.2. (a) Device structure of TFT. a-IGZO channel layer deposited on a plastic substrate. (b) Hall mobility of amorphous and crystalline IGZO films. [1]

1.2. Instability issues in amorphous semiconducting oxide

While AOSs are promising alternatives to Si-based-materials for application to active layer of TFTs in display device, many researches have reported various instability issues of the oxide semiconductor TFT. In general, the oxide semiconductors are transparent and do not absorbed the most of photons within visible range due to large optical band gap, but it was reported that the visible and UV light illumination on the AOS TFT creates a considerable amount of the photocurrent and the photo-induced conducting state remains for hours or days, even in the absence of light as shown in Fig. 1.3. (a). This long-lived photo-conducting state is called persistent photoconductivity (PPC) and it has been known as a critical disadvantage of oxide semiconductor TFT. [8-10] In addition, experimentally, the threshold voltage (V_{th}) shift of the oxide semiconductor TFT has been observed under gate bias stress conditions. Specifically, Fig. 1.3. (b) show that the application of the positive gate bias for turning on the TFT leads to a positive shift in the V_{th} and the impact of the negative gate bias is in reverse as shown in Fig. 1.3. (c). [11,12] Besides, the illumination of visible and UV light accelerates the negative shift in V_{th} under the negative gate bias condition and the transfer characteristics of the TFT is

deteriorated increasing subthreshold swing as shown in Fig. 1.3. (d). More serious problem is that these V_{th} shifts are not recover right after removing the gate bias stress and it takes hours or days for full recovery. As a result, this slow recovery of V_{th} shift is considered as a major hurdle to be solved for long-term stability of AOS in TFT.

Several mechanisms are suggested to understand origins of these phenomena. Some earlier studies addressed that these instabilities come from interface properties between TFT and insulators. [2][5] It seems clear that interface states are related to the instability, but understanding the microscopic structures of the interfaces remains to be unresolved. If interface states are formed to be deeply located within the band gap or formed as tail states, electrons or holes can be trapped under applied stresses, but the microscopic nature of interface states has not been revealed clearly yet.

Some researches suggest that it is suggested that V_O in bulk can be transformed into charged state V_O^{2+} by visible-light photo-excitation when electrons and holes carrriers excited and generated under illumination stress, then the holes can be accumulated in interface by negative bias field, and finally V_O near the interface acts as the hole trap sites. [6]

On the other hand, the electron trap sites, also may exist near the interface of insulator and AOS, and if then, it affects positive shift of threshold voltage.

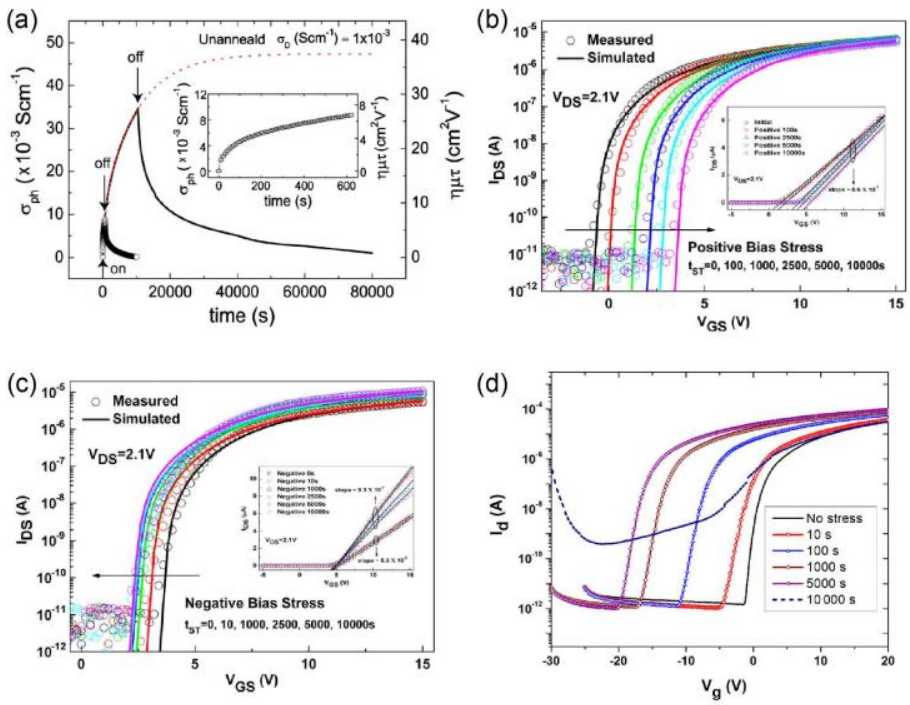

Figure 1.3. (a) Persistent photoconductivity in IGZO. [8] (b) and (c) show transfer characteristics with positive and negative shift of the threshold voltage under positive and negative bias stress, respectively. [11] (d) The variation of transfer curve under 410 nm light illumination with −20 V gate bias. [12]

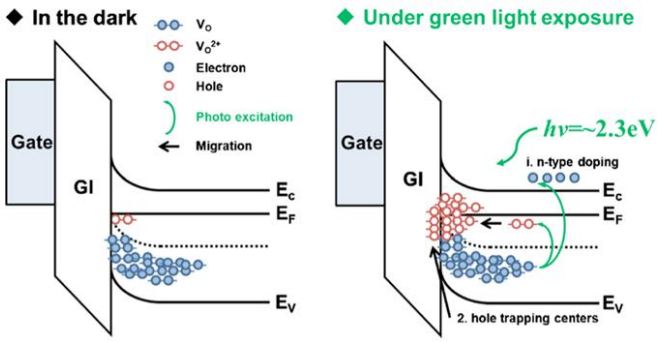

Figure 1.4. Interface hole traps that made of V_O. [13]

1.3. Overview of V_O researches on amorphous semiconducting oxide

The role of V_O in the device instability critically depends on its nature, specifically, whether defect levels associated with V_O is shallow or deep. For instance, according to a widely cited mechanism [14], V_O is a deep donor and becomes ionized under visible light. The ionized V^{2+}_O defect then migrates towards the interface with gate dielectrics under the negative bias and becomes hole-trapping sites, sustaining the threshold-voltage shift. On the other hand, if V_O belongs to the shallow donor, it would increase the electrical conductivity but may not be directly involved in NBIS instability. Because of experimental difficulty in isolating the property of point defects, the density functional theory (DFT) calculations have been useful in investigating V_O in a-IGZO. [14-21] However, the conclusion on the nature of V_O is sharply divided; while V_O was found be dominantly deep in Refs. 14, 15, 16, shallow property was also claimed in Refs. 17, 18, 19. (Ref. 20, 21 is inconclusive.)

In ref. 17 T. Kamiya et al. made the stoichiometric a-IGZO models by MQ simulation using classical MD, and the relaxation was done in LDA with VASP code. They made oxygen deficient models through removing an oxygen ion in the models, they got both of shallow donor defects which have outward relaxation and deep defects which have inward relaxation. And they reported $E_f(V_O)$ is 3.3-4.7 eV, In coordinated to V_O tends to decrease the $E_f(V_O)$ on the contrary Ga tends to increase that.

In ref. 15 Ryu et al. made oxygen deficient model using GGA and GGA+U as implemented in VASP code. They reported that in some cases shallow defects is also formed but most V_O defects have deep donor levels induced by inward relaxation. Because $\epsilon^{+2/0}$ levels are located at quite above the CBM, V_O^{+2} is very stable and hole accumulation near the interface could be occur under negative gate bias.

In ref. 14 H.-K.Noh et al. did hybrid functional calculations, they reported most V_O defects have deep donor levels and average $\epsilon^{+2/0}$ levels are beneath the band gap except V_O samples with the Ga-Ga bonds. Also they performed MD calculation within GGA+U to examine the effect of thermal annealing on the recovery process. In 8ps, 6 V_O^{+2} samples were heated up from 200 to 400°C, 4 of them recovered their original neutral configurations.

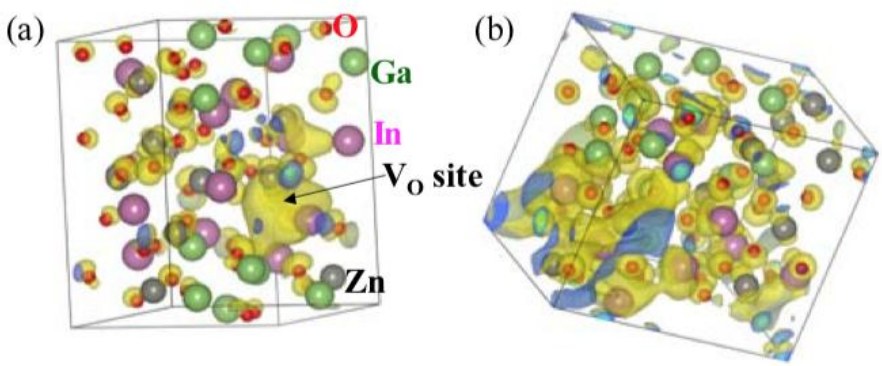

Figure 1.5. Norms of HOMO wave functions (yellow surfaces show iso-surfaces and blue areas show their cross-sections) for oxygen deficient a-IGZO obtained by LDA calculations. (a)Model 1, and (b) Model 2. Purple, green, grey and red spheres represent In, Ga, Zn and O ions, respectively. [17]

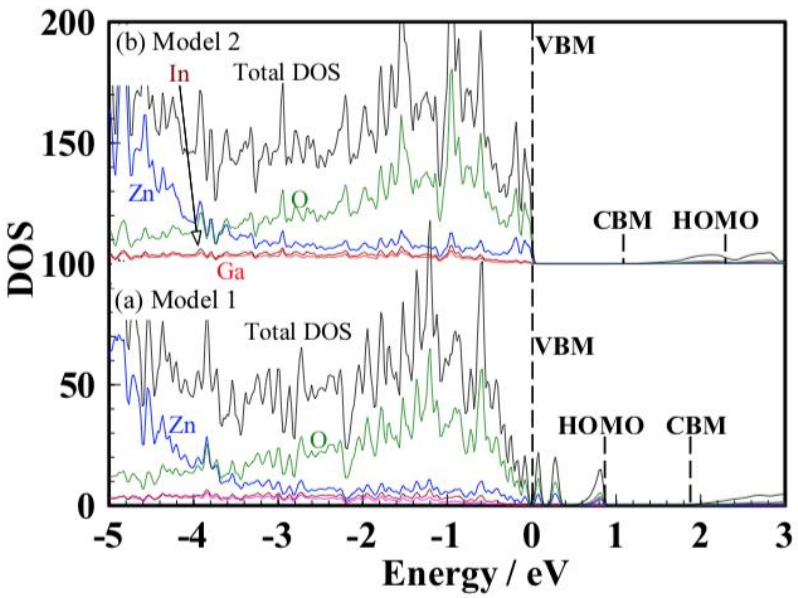

Figure 1.6. Calculated DOSs of oxygen deficient a-IGZO. (a)Model 1, and (b) Model 2. The energy is measured from theVBM.

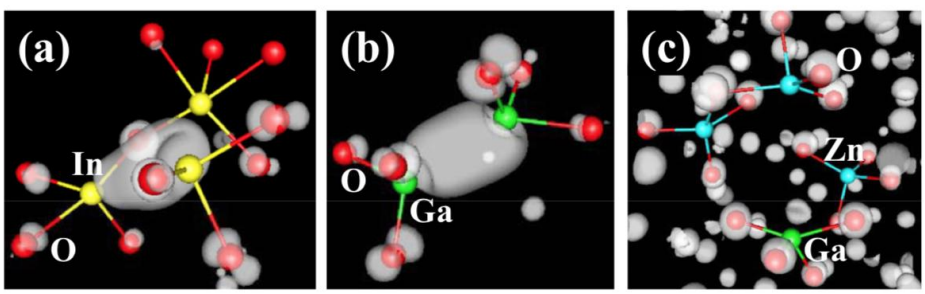

Figure 1.7. Isosurfaces of the charge densities for the deep levels of V_O, with the (a)In or (b) Ga atoms in the neighborhood, and (c) the shallow V_O defect surrounded by one Ga and three Zn atoms, with electrons in the CBM. [15]

In ref. 18 A. J. Meux et al. used classical MD in MQ simulation and PBE+U within quantum espresso to calculate relaxation. In their result, shallow defect is more favorable than deep defect. They insist that sample size that previously used (84 atoms) is not sufficient and at least more than 105 atoms are needed. Only 45% of V_O makes localised stated induced by M-M bonds, and most of their $\epsilon^{+2/0}$ levels are located above the CBM.

In ref. 19 I.-J. Kang et al. tested several supercells containing 56, 84, and 112 atoms within PBE+U. They reported that cell size dependence between 84 and 112 atoms cells is weak and they could not find any localized states around CBM.

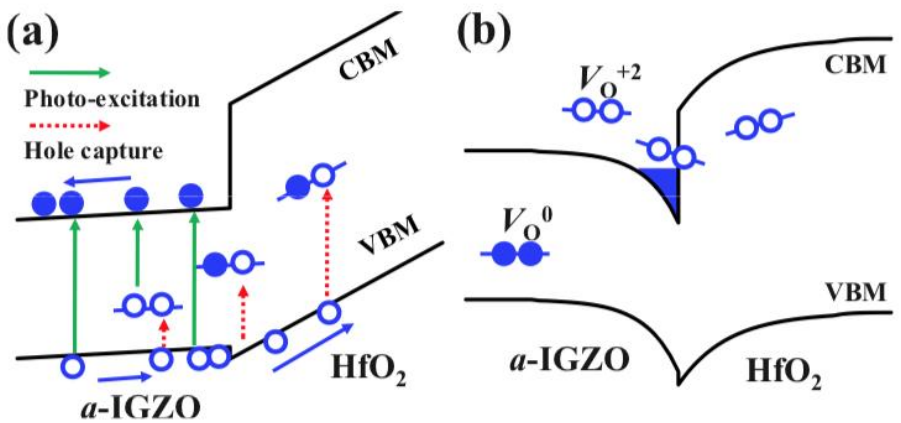

Figure 1.8. Schematic illustrations of the photoexcitation of electron-hole pairs and the V_O defects, the drift motion of hole carriers, the hole trapping in the channel/dielectric interface (a)under the NBIS and (b) after switching off the NBIS. In (b), a potential well is developed due to the band bending at the interface.[14]

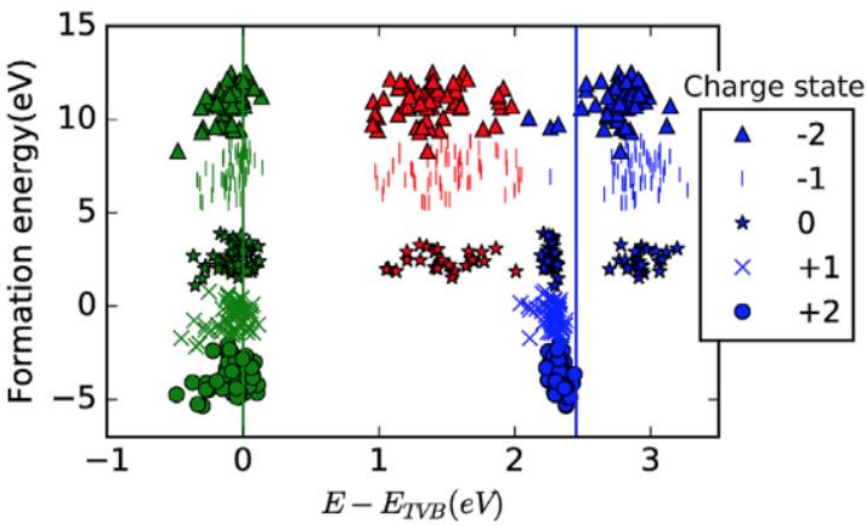

Figure 1.9. Distribution of the signature of the localized Kohn-sham states for 60 different models of an oxygen deficient a-IGZO and for five different charge states. The figure represents the position in energy (at gamma) of the Kohn-Sham states of the conduction band (blue), valence band (green), and of the states in the bandgap due to the localized Metal-Metal state (red) when they are present. [18]

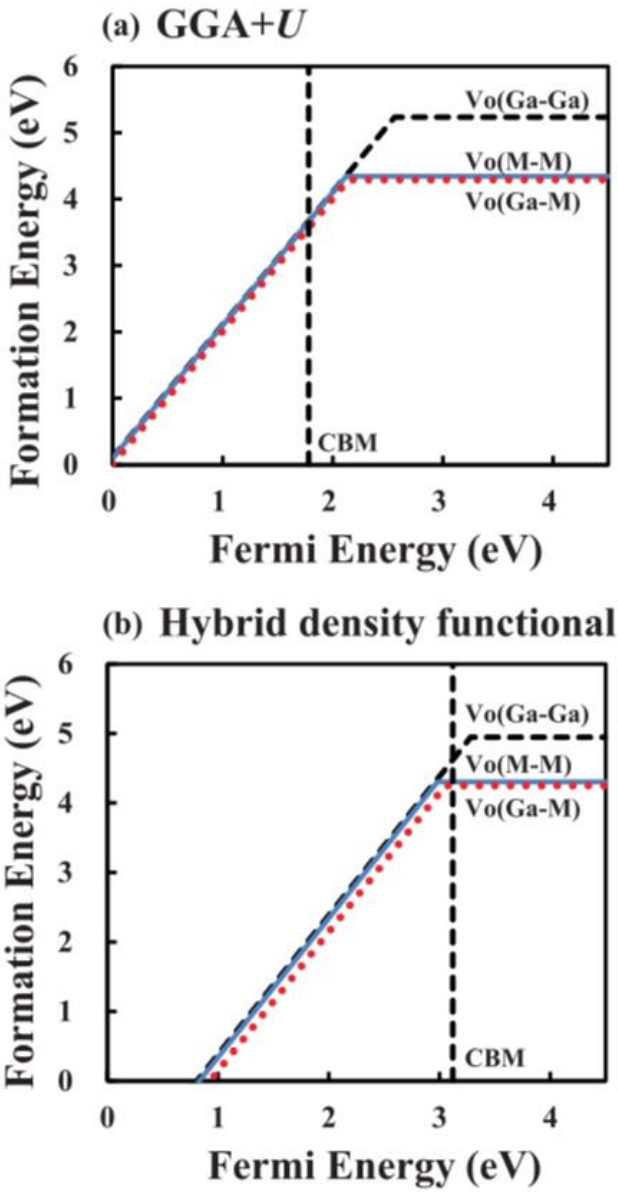

Figure 1.10. The average formation energies of V_O defects with Ga-Ga, Ga-M, and M-M bonds [V_O(Ga-Ga), V_OGa-M),and VO(M-M), respectively] as functions of the Fermi energy for the neutral and +2 charge states.[14]

1.3. Goal of the dissertation

The main purpose of this study is to reveal the microscopic origin for the illumination instability of AOSs using ab-initio calculation technique for developing AOS with high mobility as well as outstanding stability. The density functional theory (DFT) based quantum simulation method is used to understand the materials property. On the basis of the DFT calculation results, the analysis to understand the electrons behavior when a solid is exposed to the various stress conditions such as the light illumination. Among the various defects we focus on the oxygen vacancy especially, and the interface structures between channel/dielectric layers and oxygen vacancy at the interfaces.

The nature of oxygen vacancy (V_O) in the amorphous oxide semiconductor $InGaZnO_4$ (a-IGZO), which has not been fully clarified despite its technological importance. The oxygen-deficient amorphous structure models are generated through the full hybrid functional molecular dynamics (MD) simulations that allow for finding stable V_O configurations while minimizing computational approximations, which would give more accurate results.

In order to identify the source of charge trapping sites causing the device instability, we carry out ab initio calculations on the interface

between amorphous SiO_2 and a-IGZO. We try to figure out charge trapping sites exist at the stoichiometric interface, or oxygen vacancies at interfaces.

CHAPTER 2

Theoretical background

2.1. First-principles calculation : density functional theory (DFT)

2.1.1 Hohenberg and Kohn theorem

First-principles calculation is a computational method based on the level of established laws of physics not to need any empirical models obtained from experiment or fitting parameters. In most cases, the established law used in physical simulations is quantum mechanics.

$$H = \sum_{i}^{Na} - \frac{\hbar^2 \nabla_i^2}{2M_i^2} + \frac{1}{2}\sum_{i=1}^{Na}\sum_{j\neq i}^{Na} \frac{Z^2 e^2}{\left|\overrightarrow{R_i} - \overrightarrow{R_j}\right|} \qquad (2.1)$$
$$+ \sum_{k}^{N_e} - \frac{\hbar^2 \nabla_k^2}{2M_i^2} + \frac{1}{2}\sum_{k=1}^{N_e}\sum_{l\neq k}^{N_e} \frac{e^2}{\left|\overrightarrow{r_k} - \overrightarrow{r_l}\right|} - \sum_{i=1}^{Na}\sum_{k=1}^{N_e} \frac{Z^2 e^2}{\left|\overrightarrow{r_k} - \overrightarrow{R_i}\right|}$$

Eq. (2.1) is the Hamiltonian of solid materials which have periodic

positive ions and electrons move around them. $\left(\overrightarrow{R_i}, \overrightarrow{R_j}\right)$ and $\left(\overrightarrow{r_k}, \overrightarrow{r_l}\right)$ represent position of ions and electrons, respectively, Ze is the nuclear charge of ion, $\left(M_i, m\right)$ are the mass of the nuclei and electron, respectively. First two terms are the kinetic energy of ions and the potential energy between ions, and third and fourth terms corresponds to the kinetic energy of electrons and the potential energy between electrons respectively. The last term represents the potential energy between electrons and ions. For describing the motion of electrons, the first two terms in Eq. 2.1 can be ignored in practical, and they are separately treated. Because the mass of a ion is much heavier than that of an electron, the characteristic velocity of a nucleus is much slower in comparison with that of an electron. This is the Born-Oppenheimer approximation and the Hamiltonian becomes

$$H = \sum_{k}^{N_e} - \frac{\hbar^2 \nabla_k^2}{2M_i^2} + \frac{1}{2} \sum_{k=1}^{N_e} \sum_{l \neq k}^{N_e} \frac{e^2}{\left| \overrightarrow{r_k} - \overrightarrow{r_l} \right|} - \sum_{i=1}^{Na} \sum_{k=1}^{N_e} \frac{Z^2 e^2}{\left| \overrightarrow{r_k} - \overrightarrow{R_i} \right|} \quad (2.2)$$

This Hamiltonian is many-body problem except for one hydrogen atom model and there is no analytic solution for the equation.

To resolve the trouble, density functional theory (DFT) is introduced by Hohenberg and Kohn in 1960s. [22] The essential point of this theorem is that a functional of ground state charge density $\rho(r)$ is necessary

and sufficient condition to determine the electronic structure and the energy of the system. We are able to calculate charge density and wave function solving the Schrödinger equation. The total energy E of the system is given by the following equation:

$$E[\rho] = F[\rho] + \int \rho(r) V_{\text{ext}}(r) dr \tag{2.2}$$

with

$$F[\rho] = T[\rho] + U_{\text{ee}}[\rho] \tag{2.3}$$

where F is the universal functional, V_{ext} is the external potential, T is kinetic energy and U_{ee} is electron-electron interaction energy. It can be proven that the total energy in Eq. (2.2) is minimum when $\rho(r)$ corresponds to the real ground state charge density.

2.1.2 Kohn-Sham equation

The Hohenberg and Kohn theorem made the many-body equation much simpler, but the equation is still unsolvable because of the high degree of freedom generated by electron-electron interaction. In 1965, Kohn and Sham suggested effective potential V_{eff} to solve the many-body system. [23] In the theorem, electron-electron interactions are considered as an effective potential $V_{eff.}$. In other words, we consider the interactions between many-body as the interaction between one electron and $V_{eff..}$.

$$V_{\mathrm{eff}}(r) = V_{\mathrm{ion}-e} + V_{e-e} + V_{xc} \tag{2.3}$$

V_{ion-e} is the ion-electron interaction energy (Ewald energy), V_{e-e} is the electron-electron coulomb interaction energy (Hartree energy) and V_{xc} is the exchange-correlation potential which is related to the many body system. As we introduce the effective potential, the Schrödinger equation becomes simple one particle equation.

$$\left[-\frac{\hbar^2}{2m}\nabla^2 + V_{\mathrm{eff}}(\rho(\vec{r}))\right]\psi_i(\vec{r}) = \epsilon_i\psi_i(\vec{r}) \tag{2.4}$$

Eq. (2.4) is the Kohn-Sham Hamiltonian established with effective potential. It consists of kinetic energy term and effective potential term. Starting with trial charge density and wave vectors from atomic potential of the system, the effective potential can be calculated and then the equation became an single particle equation. By then the Fermi energy and new charge density is determined. This procedure should be consistently repeated until the new charge density became exactly same with given charge density. In practical, we check the difference between two densities and we consider the two densities are identical when the difference becomes smaller then given criteria.

2.1.3 Exchange-correlation energy

So, determining of effective potential is very important in the DFT theorem. V_{xc} is related to the many body system, and it can be generated by different approximations.

One of the method is local density approximation (LDA). LDA was suggested by Kohn and Sham.[23] It assumed that the exchange-correlation energy of the system is identical to that of the homogeneous electron gas. By the approximation, the exchange-correlation potential just depend on the local density of the system.

$$E_{xc}^{LDA}[\rho(r)] = \int \epsilon_{xc}^{LDA}(\rho(r))\rho(r)dr \tag{2.5}$$

The LDA is suitable for calculating the systems that have smooth electron density such as the free electron like models. However, it is not adequate for using the systems that have rapidly changing electron density such as the transition metal.

In order to overcome the problem, generalized gradient approximation (GGA) was introduced by Perdew[24] and Becke[25]. The GGA considers

not only electron density of local points but also gradient of electron density to calculate the exchange-correlation energy. This advance makes the description of rapidly changing electron density accurate. Perdew-Burke-Ernzerhof[26] potential is one of the most popular GGA potentials and uses the equation below to express the exchange-correlation energy.

$$E_{xc}^{GGA}[\rho(r), \nabla\rho(r)] = \int \epsilon_{xc}^{GGA}(\rho(r), |\nabla\rho(r)|)\rho(r)dr \qquad (2.6)$$

GGA functional commonly improves the results like energetics, bond length, compared to that of LDA.

2.2 Beyond DFT

2.2.1 DFT+U

In the LDA and GGA scheme, DFT have artifacts with describing strongly correlated system, because self-interaction error is not canceled. Electrons in *d* or *f* orbital have natures localized but in GGA because of self-interaction electrons tends to be delocalized. To resolve this obstacle, DFT+U formalism is developed.[27] The DFT+U formalism adds on-site Coulomb interaction term U and on-site Exchange interaction term J to specific orbital, and the value of U and J should be identified empirically.

$$E_{local}^{DFT+U} = E^{DFT} + \frac{1}{2}U\sum_{i\neq j}\rho_i\rho_j - E^{ee},$$
$$E^{ee} = \frac{UN^2}{2} - \frac{1}{2}\sum_{\sigma}N_{\sigma}^2 - \frac{1}{2}(U-J)\sum_{\sigma,m}n_{m,\sigma}^2. \quad (4)$$

The DFT+U calculation generally gives more accurate electron structures or energetics, but some times gives worse bond length than DFT.

2.2.2 Hybrid functional

The conventional DFT schemes such as LDA and GGA successfully describe the various materials properties including structural, mechanical and electronic properties. But the both LDA and GGA intrinsically fail to predict the band energy level, which is well known as band gap underestimation. The main reasons of the problem are that omission of self-interaction and derivative of exchange-correlation energy.

The hybrid functional can give more realistic band gap than conventional DFT results.[28] The exchange correlation functional in the hybrid functional scheme are estimated by mixing the exact exchange energy from Hartree-Fock (HF) theory and that from conventional DFT. The self-interaction error in the DFT scheme is reduced by HF theory. We apply HSE06 method[29]. In HF method, the exchange energy is exponentially decaying as a function of distance and we can exclude long-range (LR) part. The exchange energy in HF method requires high computational cost since it is estimated by integrating the orbital directly. Thus, excluding LR part lead to the improvement of computational efficiency. The exchange energy in HSE06 method is defined as

$$E_{xc}^{\mathrm{HSE}} = \alpha E_x^{\mathrm{HF,SR}}(\mu) + (1-\alpha) E_x^{\mathrm{PBE,SR}}(\mu) + E_x^{\mathrm{PBE,LR}}(\mu) + E_c^{\mathrm{PBE}} \qquad (2.7)$$

where α is mixing parameter and μ is the screening parameter, the criteria for splitting short-range (SR) and LR. We choose 0.25 as α and 0.2 Å^{-1} as μ.

In the most case, HSE06 calculation gives improved band gap close to the experimental gap. However, it still underestimate band gap of some cases especially high band gap materials for example, a-IGZO$_4$. In this work, improved band gap is obtaion by adjusting the mixing parameter.

2.3. Inverse Participation Ratio (IPR)

The degree of delocalization can be quantified by the inverse participation ratio (IPR) as follows:

$$\mathrm{IPR} = \frac{\sum_i^N w_i^2}{\left(\sum_i^N w_i\right)^2}, \tag{6}$$

where N is the total number of atoms in the supercell and w_i is the partial weight of the given state on the i-th atom. If the state is evenly distributed over entire atoms, IPR becomes 1/N, [30] while it approaches one when it is localized over a few atomic sites. Based on the definition of IPR in Eq. 6, if some defect state develops a dispersive band with low IPR values, it is regarded as shallow, while the flat band with high IPR indicates the deep character.

2.4. Defect formation energy

In the supercell formalism, defect formation energy of a charged defect can be evaluated by following equation.

$$E^f(q) = E^d_{tot} - E^b_{tot} + \mu_d + q(\mathrm{VBM} + E_F) \quad (7)$$

where q is the charge state, Ni and μ_d are the number and chemical potential of the chemical species d. In Eq. (7), E_F indicates the Fermi energy with respect to the energy at the valence band maximum (E_{VBM}) and The chemical potentials reflect the experimental growth condition.

CHAPTER 3

Nature of V_O in amorphous oxide semiconductors

3.1. Introduction

Calculating amorphous structure have several problems, but they are mostly originated from subtle configuration-energy space. Unlike crystal structure, a structure model of amorphous can not represent the amorphous phase. Amorphous have very many local minima in configuration space, and they can exist in real situations. It makes the calculation take longer, because we should calculate several structure models and analyze the average properties of them.

In this chapter, we deal with nature of V_O in amorphous oxide semiconductors especially in terms of the level of donor states which should be investigated for improving the performance of the TFT. First, we are going to discuss several correction schemes which should be considered for the precise DFT calculations. One is band gap correction, which largely depends on the energy position of defect levels within the band gap. The other one is band filling correction, which plays important role in the term of energetics of defects. In addition, we will discuss influence of protocol of modeling V_O. The foregoing discussion concludes that every calculation in the literature so far suffers from its own computational limitation, which renders the discovered nature of V_O to be disputable. In this Letter, we explore the nature of V_O in

a-$IGZO_4$, addressing the above drawbacks in the previous calculations, This approach allows us to identify stable V_O configurations without any bias or constraints, while maintaining the correct band gap. In the condition which contains all the corrections, we investigate the atomic structural properties and electronic structure of V_O.

3.2. Calculation method

3.2.1 Band gap correction

The band gap from the conventional DFT is severely underestimated in post transition metal oxides; the experimental band gap is ~3.0 eV [17,31] but the local-density approximation (LDA) or generalized-gradient approximation (GGA) yield only 0.5-0.9 eV [14,20]. By applying the on-site Coulomb repulsion (so called +U method), the band gap increases to 1.4-1.8 eV [14], still far below the experimental gap. Such band-gap underestimation obscures the boundary between the deep and shallow defects, which largely depends on the energy position of defect levels within the band gap, and leads to different conclusions depending on the computational parameters. We also note that the small band gap may unduly favor shallow-type donors by discounting the energy cost for generating defect levels close to the conduction band. Indeed, hybrid functional calculations producing a large band-gap (> 3 eV) favored deep states compared to (semi)local functionals. So We employ the hybrid functional of the Heyd-Scuseria-Ernzerhof (HSE) type through the whole calculations. The fraction of the exact exchange energy is set to 0.32, tuning to the experimental band gap for crystalline $InGaZnO_4$ (3.5 eV). This produces

2.9 eV for the band gap of the stoichiometric a-IGZO, which is in good agreement with experimental values. The smaller band gap of a-IGZO than for the crystalline phase is attributed to the downshift of the conduction band, as discussed in the previous work.

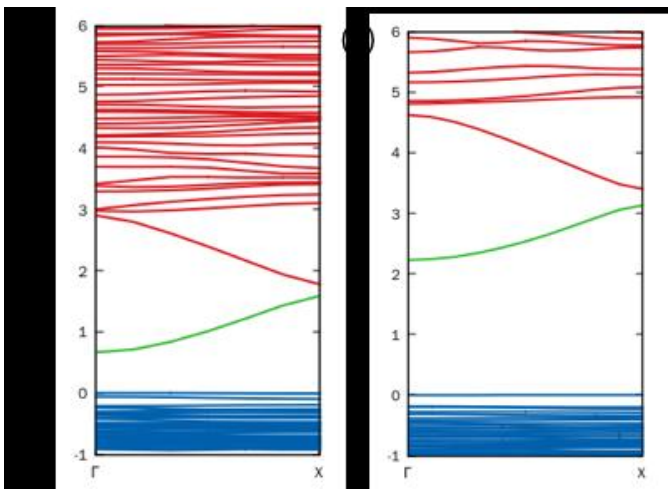

Figure 3.1. Band structures of a-$IGZO_{4-x}$ models in (a)GGA+U, (b)HSE06

3.2.2 Band filling correction

The schematic band structure diagrams of the shallow and deep donor states are shown in Fig. 3.2. A defect band have to be flat and converge to a single point in the limit of an infinitely large enough supercell, whereas it becomes dispersive in a finite supercell. For the neutral V_O, the extra two electrons remained from oxygen vacancy will occupy the defect band. The shallow level is supposed to be perturbed by the host band and have the similar dispersion with the conduction band as in Fig. 3.2(a), and the deep level is supposed to shown in the flat line within the band gap as in Fig. 3.2(b). In the limit of shallow level [see Fig. 3.2(a)], the two electrons will occupy the dispersive band and give an average energy ($E_{D,k-av}$). In the infinite cell approximation, these two electrons will only occupy state at the Γ point which has the lowest energy. However, in a calculation in a finite cell size, the electrons will occupy the defect levels at many k points, resulting in errors, which is called band-filling problem. [32]

In the $IGZO_4$, the band-filling problem becomes serious in calculations of shallow defects using a finite supercell. In shallow defects cases, the defect level seems to be severely perturbed by conduction band since the conduction band is highly dispersive and its minimum (CBM) appears at Γ. For the Brillouin-zone integration, only the Γ point is sampled,

which allows us to avoid the band-filling problem. (Note that we are aiming at identifying the defect property in the dilute limit, i.e., low oxygen deficiency.)

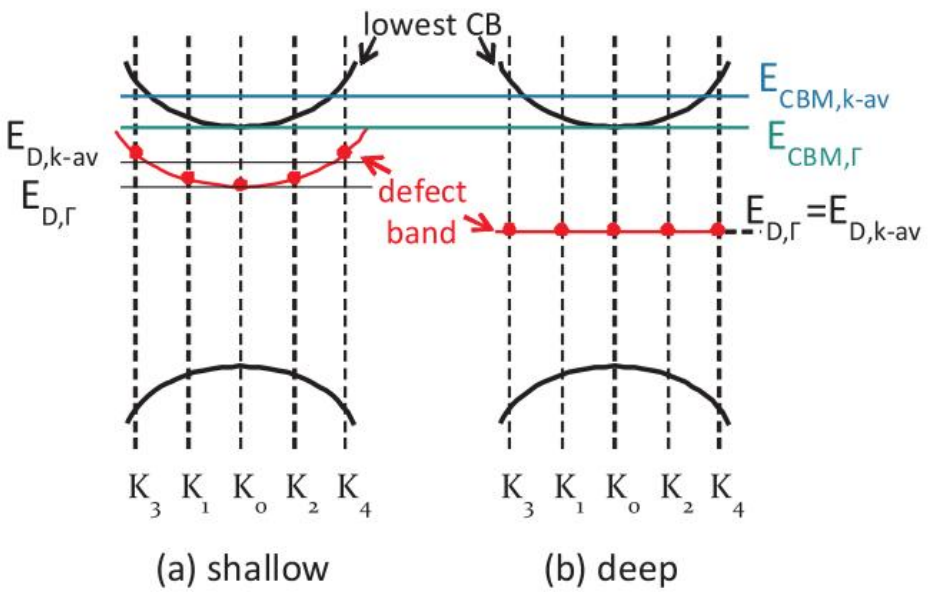

Figure 3.2. The schematic band structure of the deep and shallow V_O^0 states. The dashed lines represent the special k points used in the supercell calculations. The energy position of $E_{CBM,k-av}$, $E_{CBM,\Gamma}$, $E_{D,k-av}$, and $E_{D,\Gamma}$ are also indicated. [32]

3.2.3 Oxygen deficient melt-quench protocol

Most of the extant theoretical works modelled V_O by removing one oxygen atom from the stoichiometric a-IGZO structure that was constructed through melt-quench molecular dynamics (MD) simulations. Various defect sites were then sampled and their formation energies were compared. However, due to the inherent meta-stability of amorphous structures, the energetic comparison is not reliable, causing different conclusions among literature. Furthermore, such way of V_O modeling is at odds with the nature of amorphous structures that the lattice site is ill-defined. That is to say, it is conceivable in amorphous structures that V_O is structurally diffused over a large area, rather than centralized around a localized space. To take this possibility into account, it is necessary to include the oxygen deficiency during generating amorphous models, for instance, melt-quench simulations.

A few works tried such approaches in modeling the oxygen-deficient a-IGZO, but the semi-local functional used in the calculation underestimates the band gap, which can bias the result.

3.2.3.1 Problem of post-removal scheme

There is another subtle configuration-energy space problem originated difficulty. In the crystals, vacancy sites are well defined, and even if vacancy structures undergo the large relaxation process vacancy site can be easily decided. And we can compare it to non-defect bulk structure models. But in amorphous structures, because of the subtle configuration-energy space of amorphous structures, the analyzing of defects configuration is very difficult. Basically distinguishing the effects of local structures like local coordination change is nearly impossible in some conditions. For example, a local configuration change can affect the whole atomic configuration of the cell. In that case, we might not specify the effect of local configuration change. This kind of problem occurs especially in systems which mainly have ionic bond like a-IGZO, defining vacancy sites might be difficult. In a-IGZO, shallow donor V_O defects spread out spatially and it affects whole atoms in the cell to move around. It means that the structure model could be altered to totally different structure that are difficult to define as the defect structures of previous bulk. In crystal system, we calculate the formation energy of a defect on the condition in which every structures (including bulks, defects) have same phase. But in some cases, there are structure changes comparable to phase change in the

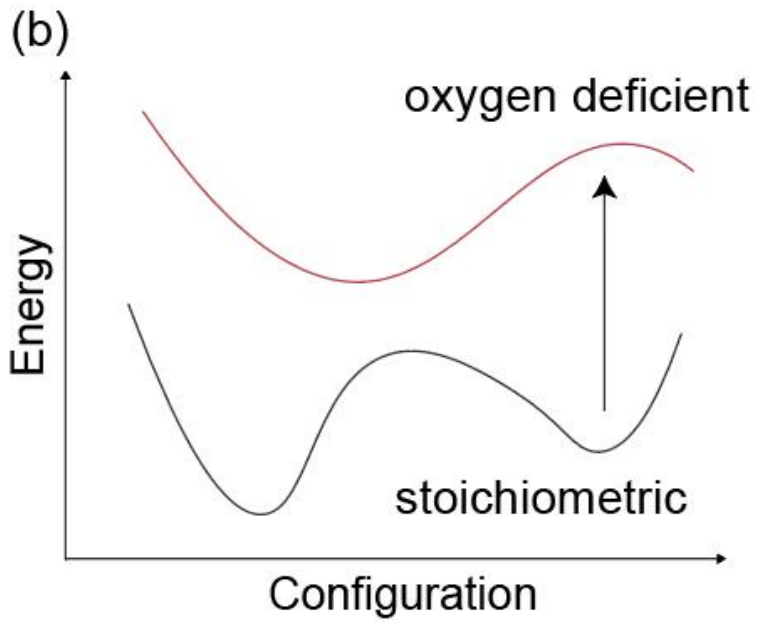

Figure 3.3. Schematic diagram of different configuration space between stoichiometric and oxygen deficient structures.

amorphous structure vacancy calculations. It seems to that stoichiometric and oxygen deficient structures exist in different configuration space. Non-stoichiometric melt-quench process can be alternative because oxygen deficient structure can search on right configuration in long time during melt-quench process.

3.2.4 Computation details

Throughout this work, the first-principles MD simulations are conducted using the Vienna Ab inito Simulation Package (VASP) [20] with the projector-augmented wave (PAW) pseudopotential. Amorphous structures for both stoichiometric a-IGZO and oxygen-deficient a-$IGZO_{4-x}$ are generated using the conventional melt-quench process.

The a-$IGZO_4$ model contains sixteen $InGaZnO_4$ units (112 atoms in total) and an oxygen atom is removed in a-$IGZO_{4-x}$ (111 atoms). First, we put constituent atoms randomly into a cubic box with the length of 11.1 Å, which corresponds to the density of a-$IGZO_4$ in experiment. The initial atomic positions are randomized by premelting at 5000 K for 2 ps, followed by melting at 2500 K for 10 ps, and they are quenched to 500 K with a constant cooling rate of −500 K/ps. The final structure is fully relaxed until the magnitude of atomic forces are reduced to within 0.05 eV/A.

The energy cut-off for the plane-wave basis is chosen to be 250 and 500 eV for the melt-quench MD process and relaxation steps, respectively. (During the melt-quench MD, a soft PAW pseudopotential was used for O atoms, which reduced the energy cutoff. Melt-quench process does not require precise pseudopotential.) To reflect the disorder in amorphous structures in a statistical way, we obtain eight

models of a-IGZO$_{4-x}$. For the comparison purpose, we also generate two stoichiometric a-IGZO (a-IGZO$_4$) models following the same melt-quench procedure.

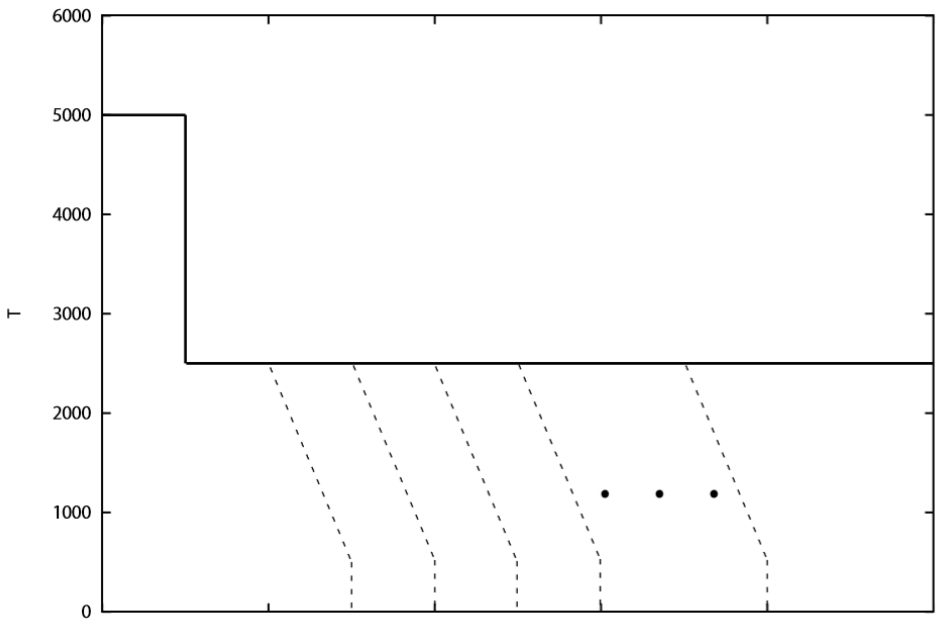

Figure 3.4. Schematic diagram of oxygen deficient melt-quench protocol. The sample in which an oxygen is removed is annealed at high temperature in long time. Then some images of the MD simulation is chosen to be quenched.

3.3. Results and discussion

3.3.1 Shallow V_O

3.3.1.1 Atomic structural

Fig. 3.5 (a) shows the pair distribution functions [g(r)] for metal-oxygen (M-O) and metal-metal (M-M) pairs that are averaged over ions within the generated models. For comparison, g(r) for a-IGZO is also shown. It is seen that the first peak is pronounced, implying that the short range order is well maintained like the crystalline phase. In Fig. 3.5 (a), g(r)' s for a-$IGZO_{4-x}$ and a-$IGZO_4$ are almost identical, indicating that the oxygen deficiency does not cause any substantial change in the amorphous structure, for instance additional M-M bonds. This is also confirmed by the M-O bond lengths and coordination numbers in Table 3.1, which shows similar results between a-$IGZO_4$ and a-$IGZO_{4-x}$. They are also in good agreements with previous theoretical results using the semilocal functional and EXAFS analysis. In Fig. 3.5 (b), we visualize voids in an a-$IGZO_{4-x}$ model following the Connolly analysis, which may enable us to identify any distinct vacancy site. However, it is seen that disjointed cavities are distributed over the supercell and the void that

can be regarded as the vacancy site is not found. This is consistent with the structural similarity between a-IGZO and a-$IGZO_{4-x}$ discussed above.

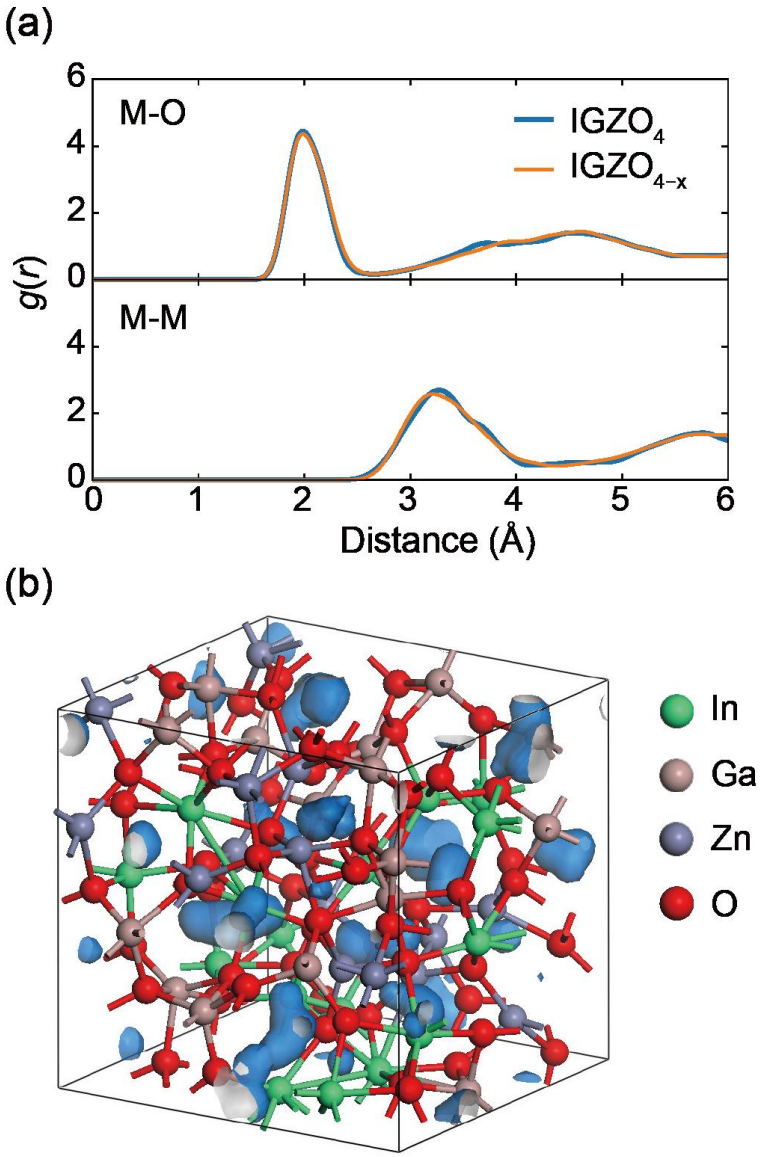

Figure 3.5. (a) Ion-averaged pair distribution functions for metal-oxygen (M-O) and metal-metal (M-M) pairs in a-$IGZO_{4-x}$ and a-$IGZO_4$. (b) Cavities in an a-$IGZO_{4-x}$ model identified by the Connolly analysis.

	This work		Cal.		Exp.	
	r (Å)	N_c	r (Å)	N_c	r (Å)	N_c
In-O	2.17 (2.17)	5.79 (5.95)	2.19	5.58	2.30	5.80
Ga-O	1.90 (1.91)	4.89 (4.85)	1.93	4.71	1.93	4.90
Zn-O	1.99 (2.00)	4.51 (4.39)	1.98	4.28	1.99	4.50

Table 3.1. Averaged values of the bond length (r) between metal and oxygen ions and coordination numbers (N_c) around metal ions in a-$IGZO_{4-x}$. The values in the parenthesis are for a-$IGZO_4$. [33,34]

3.3.1.2 Electronic structure

Even though the present work consistently employs the hybrid functional, we find that the small supercell still prohibits clear-cut distinction of the defect type. In particular, the electronic coupling between highly dispersive conduction state and localized state can make it difficult to assess the defect type purely based on the energy of defect levels. In order to draw a definite conclusion, we determine the nature of V_O by examining the band dispersion and spatial distribution of the highest occupied state, in addition to its energy level within the band gap. (Strictly speaking, the Bloch vector is not well defined in the amorphous structure. However, pseudo band-structures of the given supercell are useful to examine the delocalization. The degree of delocalization can be quantified by the inverse participation ratio.

The band structure of a-$IGZO_4$ is plotted in Fig. 3.6 (a). The valence band consists of mainly O-p states, while metal s states comprises the conduction band. The bands near the valence band maximum (VBM) exhibit flat dispersions, implying those states are spatially localized over a few atomic sites. This is consistent with the high IPR values in the right figure. This arises from inefficient hybridization between O-p states in disordered structures due to the directionality and the small size of O-p orbitals. In contrast to the valence band, the lowest

conduction band shows a significant dispersion because the overlap between the large and spherical metal s states is insensitive to the directional disorder. In particular, the well-ordered first coordination shell results in a quasi-linear conduction band, which is generally discovered in oxides containing In, Ga, Zn, and Sn. The low IPR values is much lower than for those around VBM, supporting the delocalized nature.

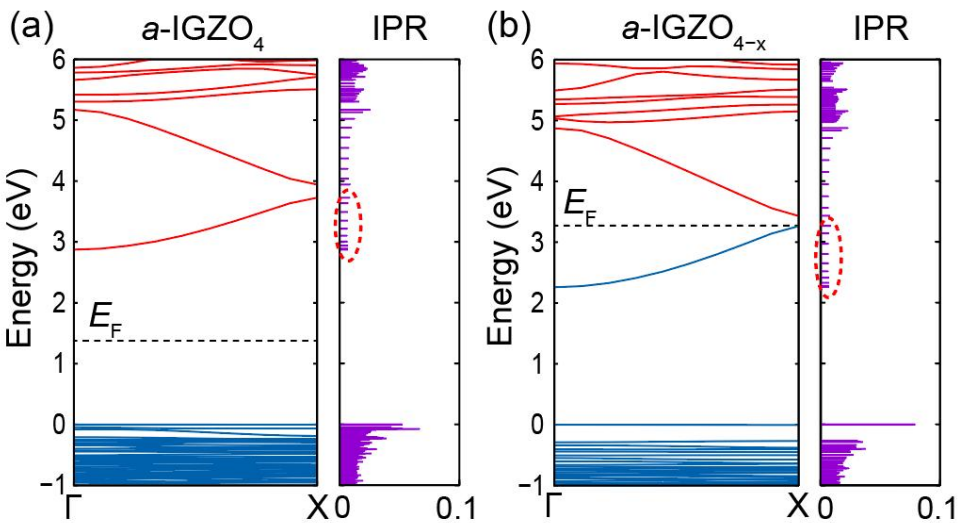

Figure 3.6. (a) Calculated band structure and IPR for a deep V_O model. The arrow indicates the deep state associated with V_O and its IPR values are marked in dashed ellipsoid. Isosurface in (b) is the distribution of the charge density of the deep level.

The band structure for an a-IGZO$_{4-x}$ model is shown in Fig. 3.6 (b). It is seen that the band structure is similar to that of a-IGZO$_4$ in Fig. 3.6 (a), and no pronounced defect level is identified within the band gap. The lack of an oxygen atom results in two electrons occupying the conduction band, raising the Fermi level above the CBM. The IPR values for the highest occupied band are similar to the CBM in Fig. 3.6 (a). This implies that the oxygen vacancy act as shallow donors. For every eight model of a-IGZO4−x, we consistently obtain the electronic structure similar to Fig. 3.6 (b), confirming the shallow nature of V_O unequivocally.

3.3.2 Deep V_O

For the comparison purpose, we artificially generate deep V_O by charging the supercell with two extra electrons during the melt-quench simulation. The extra electrons facilitate the formation of a deep level, which helps reduce the band energy. At the end of the melt-quench simulation, we remove the additional electrons and carry out the structural relaxation. Out of eight trials, we obtain five a-$IGZO_{4-x}$ models that develop a deep V_O state. Figure 3.8 (a) exhibits the band structure for one of the deep V_O models. The deep defect level is clearly seen within the band gap. The IPR value in the dashed ellipsoid indicates strong localization. This can be directly confirmed by the charge density distribution of this state in Fig. 3.8 (b). It is found that the state is well confined between two In atoms that are separated by 2.9 Å. The region at which the defect state develops does not accompany a large void that can be captured by Connolly analysis. For other cases, the deep level always develops at weak bonding between metal atoms involving at least one In atom. This is consistent with previous calculations that the defect formation energy is lower when V_O is surrounded by In atoms. This finding is not coincidental; previous calculations created V_O via the post-removal scheme and analyzed impacts of influences of the bonding enviroments on the V_O formation

energy. They revealed that the defect formation energy is lower when V_O is surrounded by In atoms. Among the five models, defect levels are scattered over 1.7-2.1 eV from CBM.

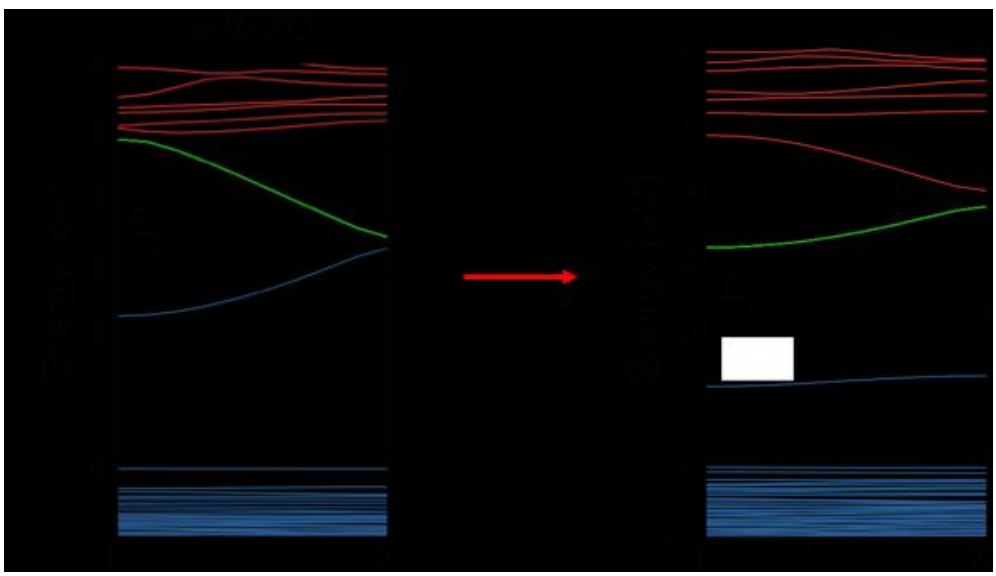

Figure 3.7. Schematic diagram of change after 2 extra electron added melt-quench process. (a) is a normal oxygen deficient a-$IGZO_4$ model and green line denotes the level which 2 extra electron would occupy. During melt-quench process, a-$IGZO_{4-x}$ would change atomic structure to reduce the energy of 2 extra electron. In the result, a deep level defect is made.

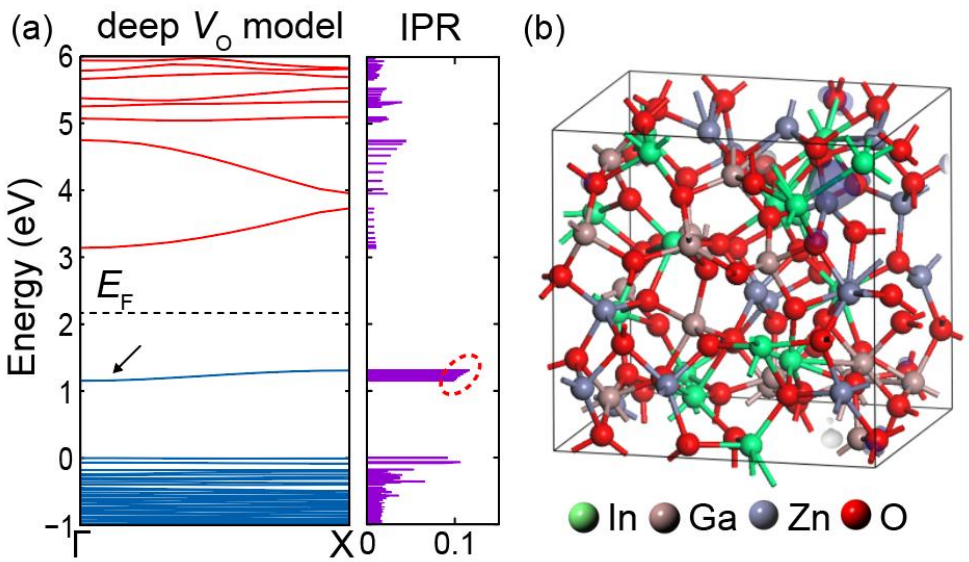

Figure 3.8. (a) Calculated band structure and IPR for a deep V_O model. The arrow indicates the deep state associated with V_O and its IPR values are marked in dashed ellipsoid. Isosurface in (b) is the distribution of the charge density of the deep level.

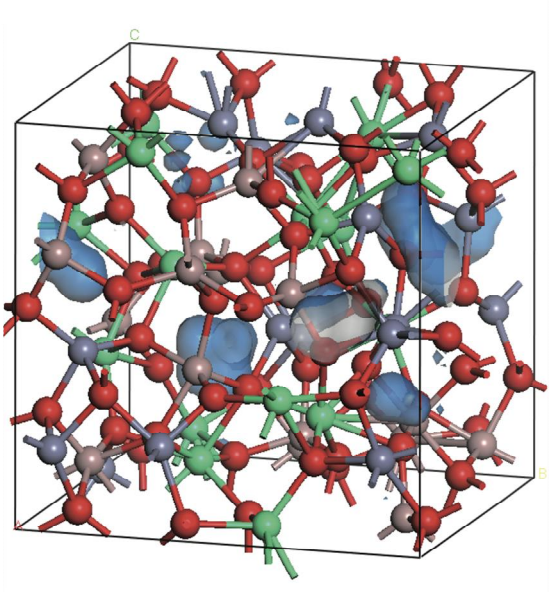

Figure 3.9. Cavities in an deep a-$IGZO_{4-x}$ model identified by the Connolly analysis.

3.3.3 Comparison between shallow and deep V_O

To compare the stability of shallow and deep V_O, we calculate the defect formation energy (E_{for}) according to the following formula:

$$E_{\text{for}} = E(a\text{-IGZO}_{4-x}) - \bar{E}(a\text{-IGZO}_4) + \mu_O, \qquad (2)$$

where E(a-IGZO$_{4-x}$) is the total energy of an a-IGZO$_{4-x}$ model and $\bar{E}$(a-IGZO4) is the average of two stoichiometric models (more sampling of stoichiometric structures would change $\bar{E}$(a-IGZO$_4$) to some extent, but it does not affect our main conclusion) . In Eq. 2, μ_O is the oxygen chemical potential, which is set to the half of the total energy of an O_2 molecule. Figure 3.10 (a) shows the calculated E_{for} for deep and shallow V_O models (five and eight, respectively). Because of the structural fluctuation in the amorphous structures, Efor varies substantially among the samples. The average energy of the shallow V_O models are more stable than the shallow V_O models by 1.22 eV, which confirms that the shallow V_O is indeed the preferred type of oxygen vacancies in a-IGZO. The relative stability can also be confirmed by the simulated annealing; for deep V_O models, we anneal the system at

600 K and find that every model converts to shallow one within 5 ps. Figure 3.10 (b) shows the schematic energy-configuration diagram for V_O in a-IGZO as inferred from the present computation.

The majority of the V_O in a-IGZO films is expected to serve as the shallow donor contributing to the n-type conductivity. This is consistent with experimental results in which a-IGZO films grown under oxygen-poor conditions exhibit higher carrier concentrations. Although metastable, deep V_O could also be present in films, but should be low in concentration. Accordingly, V_O may not be a main source causing the device instability under NBIS, and other alternative mechanisms related to hydrogen impurities or peroxide formation are therefore worth close attention.

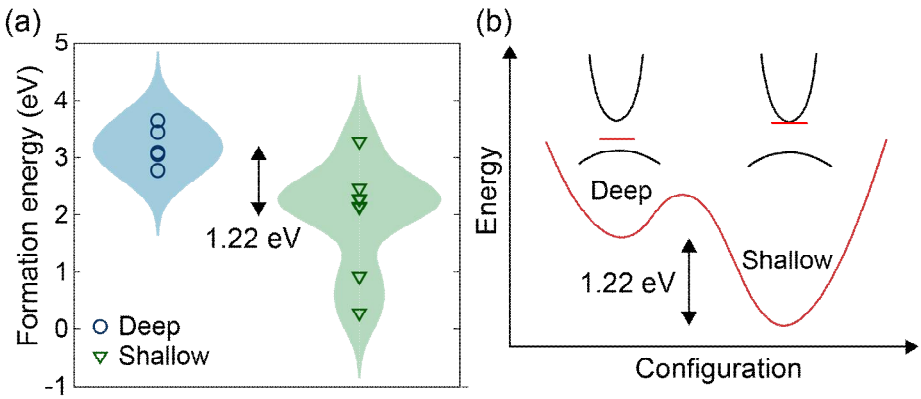

Figure 3.10. (a) Formation energy of deep and shallow oxygen vacancies. The shaded area represents the distribution of oxygen vacancy formation energy obtained by applying Gaussian broadening with a standard deviation of 0.4 eV. (b) Schematic energy-configuration diagram for oxygen
vacancies in a-IGZO.

3.3.4 Role of V_O in a-IGZO

We investigated the nature of V_O in a-IGZO using first-principles calculations. To circumvent the two modelling issues associated with the band gap and vacancy configuration, the hybrid density functional MD simulations were employed to generate oxygen deficient amorphous models. Our analysis on the electronic structure and energetics of V_O models showed that the majority of oxygen vacancies acts as shallow donors in a-IGZO.

CHAPTER 4

Modeling of the a-IGZO/a-SiO_2 interfaces

4.1. Computational details

In this work, we performed first-principles calculations using Vienna Ab-initio Simulation Package (VASP).[35] The projected augmented wave (PAW) pseudo potential method is used to describe the ion-electron interactions.[36] Because *d* electrons of In and Ga lie far below the bottom of valence band made up of oxygen *p* orbital, we treated them as core electrons. In structure relaxation steps, we used PBEsol functional since the functional gives relatively accurate bond lengths in $InGaZnO_4$ and SiO_2. On the other hand, GGA+U functional was employed when investigating the electronic structures, the atomic configurations were fixed with structures obtained with PBEsol. Treating *d* electrons of In and Ga as core electrons, effective *U* parameter was only applied to Zn *d* electrons. We used 7.5 eV as *U-J* value, where U is on-site Coulomb interactions and J is on-site Exchange interaction parameter.[37] The cutoff energy for plane-wave basis set is set to be 250 eV and 500 eV in the case of Molecular Dynamics (MD) step and structural relaxation step, respectively. When investigating electronic structures, cutoff energy is set to be 500 eV, too. We checked that in MD process the low cutoff energy of 250 eV affects trajectory of atoms negligibly. However stress tensor is very sensitive to the cutoff

energy, and the cutoff energy should be raised above 450 eV when a supercell is relaxed.

k-space mesh grid is chosen to be the single Γ-point for MD step and relaxation step, and Γ-centered $3\times3\times1$ grid during electronic structure step. Structures were relaxed until the Hellman-Feynman forces of all ions are less than 0.05 eV/Å.

4.2. Generating interface structures

To generate the interfacial structures, we first obtained *a*-SiO_2 and *a*-IGZO separately in advance. The lattice parameter of the supercells of each amorphous structure was set to a cubic box cell with 11.45 Å, and 96 and 126 atoms were included in the supercell for *a*-SiO_2 and *a*-IGZO, respectively. These corresponds to the density of 2.12 and 6.25 g/cm^3. These values are close to the experimental amorphous densities of 2.20 and 6.1 g/cm^3. Regarding the temperature protocol, pre-melting for 2 ps at 5000K, melting for 20 ps at 2500 K, and quenching to 300K with the constant cooling rate of 250 K/ps. These amorphous structures are relaxed with internal coordinates.

One can easily join the two materials because the cell parameter of two supercells are fixed and identical. The interface structures were formed by slicing and joining the *a*-IGZO and *a*-SiO_2. The slicing plane was chosen to satisfy the condition that new atomic bonds near the constructed interface are only formed between cations and anions. In this way, we made 6 interface models. The initial configuration of interfaces meets given conditions that distance between metal atoms of $InGaZnO_4$ and oxygen atoms in SiO_2 is between 1.2 and 1.8 Å. At the same time the distance between Si atoms in SiO_2 and oxygen atoms in $InGaZnO_4$ is between 1.2 and 1.8 Å. In addition, the distance between

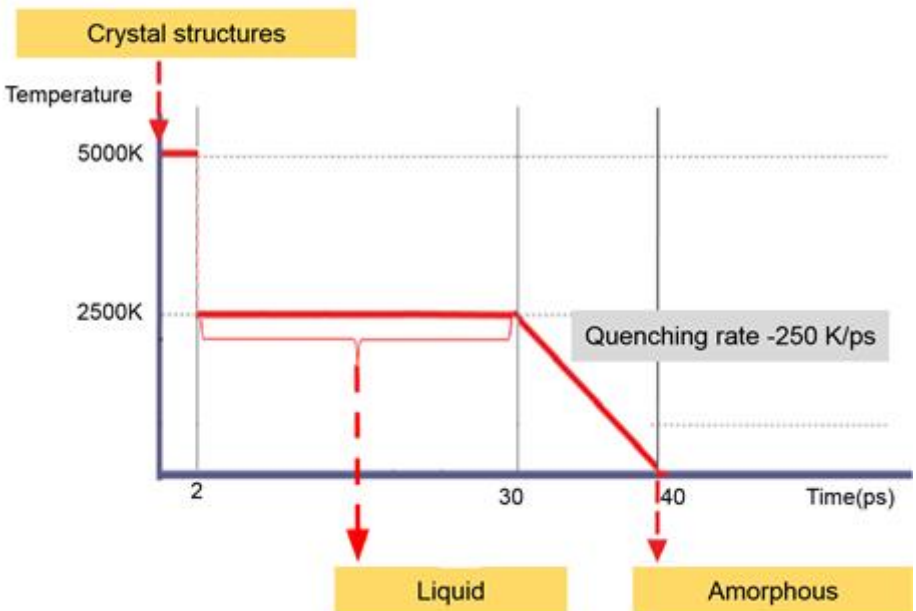

Figure 4.1. Temperature protocol of melt-quench method of making each of amorphous structures

neighboring cations or anions is longer 2.0 Å near the interface. To stabilize the interface further, the structures go through another MD simulations such that interface atoms are relaxed. We anneal the as-formed interface models at 1700 K for 4 ps followed by quenching to 300 K with the cooling rate of −500 K/ps. Finally, the structures undergo relaxation simulations at 0 K, including modification of lattice parameters. The total volume expands 2~3% during relaxation. During the interface annealing, the temperature protocol was chosen such that the intermixing is avoided. Atoms move on average by 1.3 Å during the annealing, this means that structures in the bulk part is more or less maintained.

	Slice and connect	Join and anneal
Interface Energy (mJ/cm^2)	199	419

Table 4.1. Energy difference between different methods of constructing interfaces.

This approach has several advantages. We can simply remove unrealistic bonds at interface which affect energetics and electronic structures. If we neglect considering distance between atoms near interface when making initial configuration, the possibility of formation of homopolar bonds at interface becomes extremely high, which makes annealing time longer and temperature high. Because homopolar bonds should be removed by annealing. During the annealing, atoms constructing spurious bonds should move pretty far, annealing temperature must be much higher (2500 K) than previous approach. The high temperature annealing can affect the structural features of bulk amorphous materials and it is difficult to calculate interface energy only approximately. Table 4.1 shows energy difference between former protocol (slice-and-connect) and latter protocol (join-and-anneal). Interface energy obtained from the slice-and-connect protocol would be better defined because bulk structures are maintained. In contrast the join-and-anneal protocol interfaces suffer from the alteration of bulk structures from high temperature annealing

4.3. Exchange-correlation functional dependance

DFT calculation has well-known limitations that exact exchange-correlation term can not be obtained yet. Hence we use some approximations to calculate exchange-correlation energy, and there are several approaches to evaluate that. Each of approach has advantages and disadvantages, and it is highly important to select exchange-correlation functional. In this study, two materials composing the interface have different bonding nature, we may have some difficulties in choosing the proper functional.

In, Ga and Zn constructing *a*-IGZO have *d* electrons. When we calculate oxide systems which have *d* electrons, GGA functional shows very significant self-interaction error. In oxide materials, *d* electron tends to highly localized in real system but GGA assume that every electron has tendency of being delocalized. It seems that electrons which should be localized have repulsive interaction with the electrons itself, and it become delocalized in GGA calculations. These artifact generate vast error on many properties, like energetics, bonding nature, electron structure and etc. So, we should adopt another functional, for instance GGA+U. But, in this work, GGA+U has some issues that the functional describes length of metal-oxygen bonds too tight. It is not that severe when calculating bulk properties, but in this work it seems serious. Because there is no *d* electron in *a*-SiO_2, bond length of *a*-SiO_2

shows very good agreement with experience values but *a*-IGZO does not. In interface calculations, the difference can effect as stress tensor near interface, and electronic property of interface seems sensitive to bond length of interface bonding.

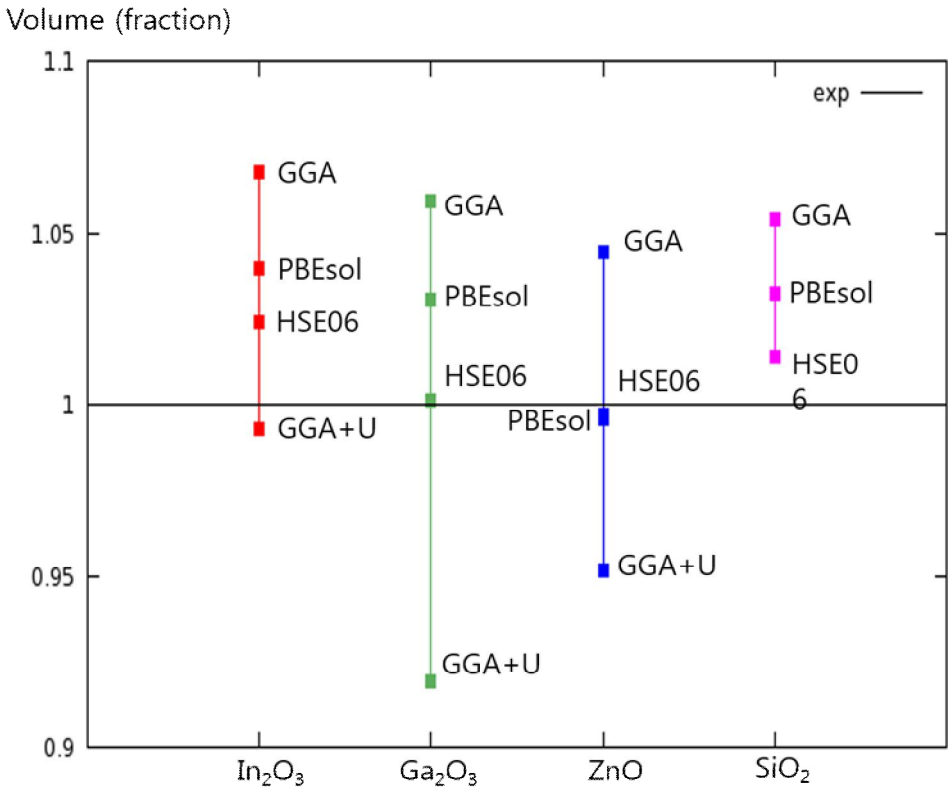

Figure 4.2. Volume dependance on exchange-correlation functional in crystal structure of In_2O_3, Ga_2O_3, ZnO, SiO_2

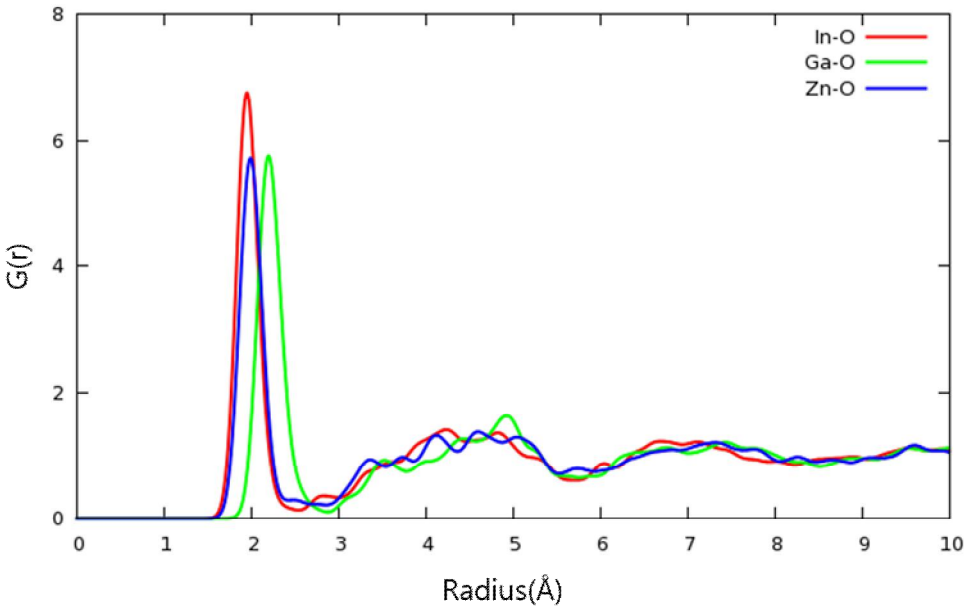

Figure 4.3. Radial distribution function of *a*-IGZO calculated by PBEsol functional

	Exp	GGA Lattice	PBEsol Lattice
In-O(Å)	2.12	2.18 (2.8%)	2.18 (2.8%)
Ga-O(Å)	1.91	1.90 (-1.6%)	1.91 (0%)
Zn-O(Å)	1.93	1.98 (3.7%)	2.03 (5.1%)
ρ (g/cm^3)	6.10	5.9	6.11

Table 4.2. Local structural parameters for *a*-IGZO with different functional

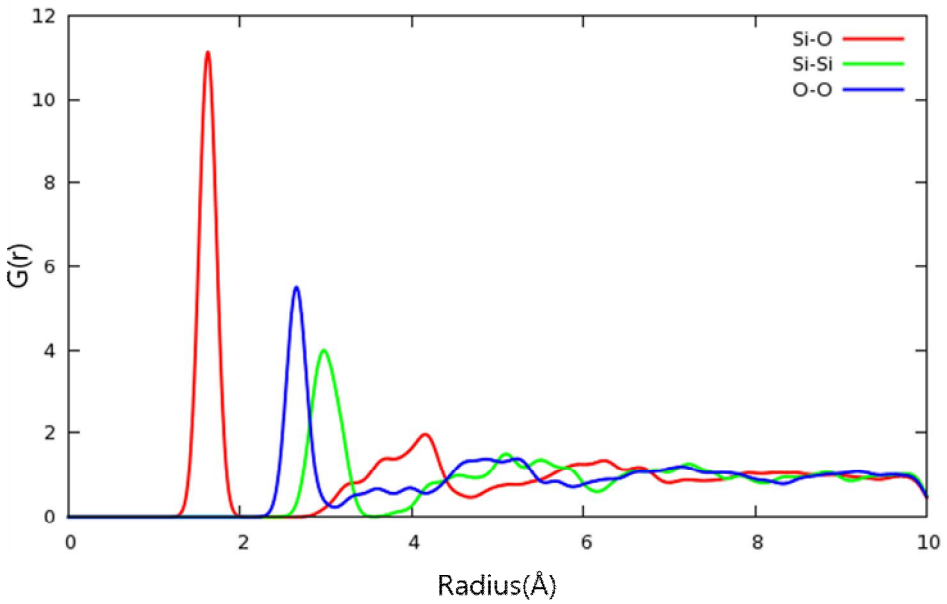

Figure 4.4. Radial distribution function of *a*-SiO_2 calculated by PBEsol functional

	Exp	GGA Lattice	PBEsol Lattice
Si-O(Å)	1.60	1.63 (1.6%)	1.62 (0.9%)
O-O(Å)	2.66	2.66 (-0.2%)	2.65 (-0.2%)
Si-Si(Å)	3.08	2.96 (-4.0%)	2.98 (-3.8%)
ρ (g/cm^3)	2.2	2.12	2.17

Table 4.3. Local structural parameters for *a*-SiO_2 with different functional

So we checked the volume of the crystalline structures dependance on functional. Fig 4.2. shows the results. It is seen that results from PBEsol show much better consistency with experimental values than GGA or GGA+U. HSE06 show most accurate results consistently but HSE06 calculation is too expensive to calculate interface relaxation, we choose the PBEsol functional. And then we applied it to each amorphous structures. Fig. 4.3. and Table 4.2 show that PBEsol give nice bond length in *a*-IGZO, Fig. 4.4 and Table 4.3 show that in *a*-SiO_2 too. Hence, we selected PBEsol functional when the atomic structure relaxation calculations step.

4.4. Character of interface atomic structures

It is seen in Fig. 4.5. that there is no homopolar bonds at the interface, indicating that two materials are well connected chemically. Oxygen atoms which compose interfacial bonds undergoes major difference of coordination numbers. Oxygens in *a*-SiO_2 have strictly two of coordination number, but in *a*-IGZO have 4~6 coordination number. When interfacial bonds are made, oxygens turn into two- or three-fold coordinated oxygen. The ratio of two-fold and three-fold oxygen is 27% and 71% on average, respectively. The average bond length at interfaces is shown in Table 4.4. The average bond length of Si-O at interface slightly differs from the bulk only by 0.02 Å. And in case of In-O and G-O bonds differ by 0.1 Å.

The average interface energy which has no homopolar bond was calculated 199 mJ/cm^2. This value is relatively low value. With respect to Fe/VN (294 mJ/cm^2)[38] and Si/$SrTiO_3$ (1433 mJ/cm^2)[39]. But the interface energy of interface models which have homopolar bond gives 913 mJ/cm^2, which is not exactly qualitative value (because they are high temperature annealed systems, and possibility of modification of bulk structures.) but we can guess how energetically unfavorable homopolar bond is.

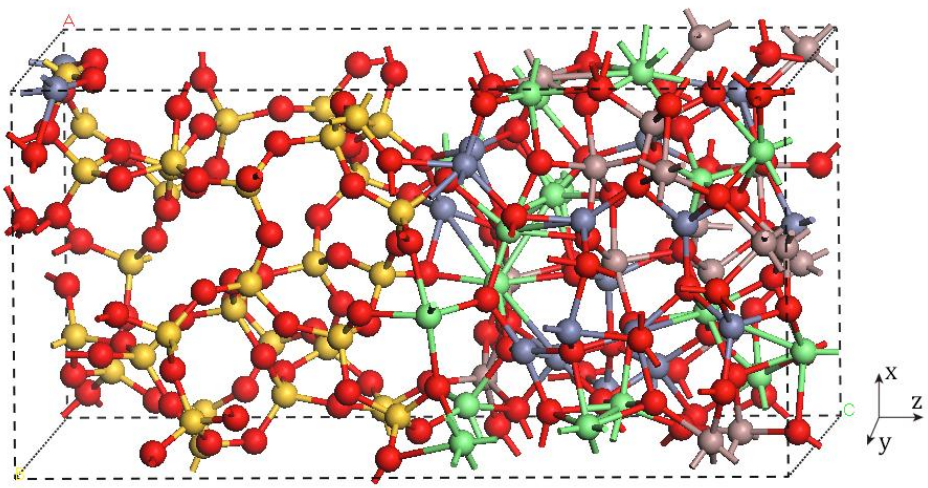

Figure 4.5. Interface model constructed by slice-and-connect method

	Bulk	Interface
In-O(Å)	2.18	2.08
Ga-O(Å)	1.91	1.81
Zn-O(Å)	2.03	2.03
Si-O(Å)	1.62	1.60

Table 4.4. Difference of the average bond length in bulk and interface

4.5. Localized states in amorphous structures

Amorphous materials have characteristic tail states. This is because amorphous structures have local disorder which induces localization of electron states. It induces subgap optical absorption significantly in amorphous materials and it can affect electronic properties of materials too.

In theoretical calculations, effect of local disorder on electronic structure is relatively well described. In most amorphous materials, energy state induced by local disorder influences the electronic structure near the band gap. But, when measuring the band gap in experiment, researchers cancel out the effect of local disorder induced tail state by introducing several method like Tauc plot gap. Therefore, in comparing the theoretical band gap value of amorphous with experimental value, we should take account into local disorder induced tail states.

In this study, *a*-SiO_2 and *a*-IGZO are both amorphous structures. Top of valence band consists of hybridized lone pair electrons of oxygen *p* orbital in both structures. But character of tail state is different because the two materials have quite different local disorder.

We checked inverse-participation ratios (IPR) as shown in Figure 4.6.

to represent the degree of localization of each state. IPR gives information on how many atoms an energy level is localized over.

IPR shows distinct discrepancy between valence and conduction edge. That is to say, IPR values near the Fermi energy shows that strongly localized states, where as conduction band states are delocalized broadly. This is because oxygen *p* orbital composing the valence band states have directionality and that makes the valence band stats very sensitive to local disorder.

The bandwidth of tail state is different with two materials, *a*-IGZO shows 0.5 ~ 0.6 eV width of strongly localized states and *a*-SiO_2 gives 0.2 ~ 0.3 eV.

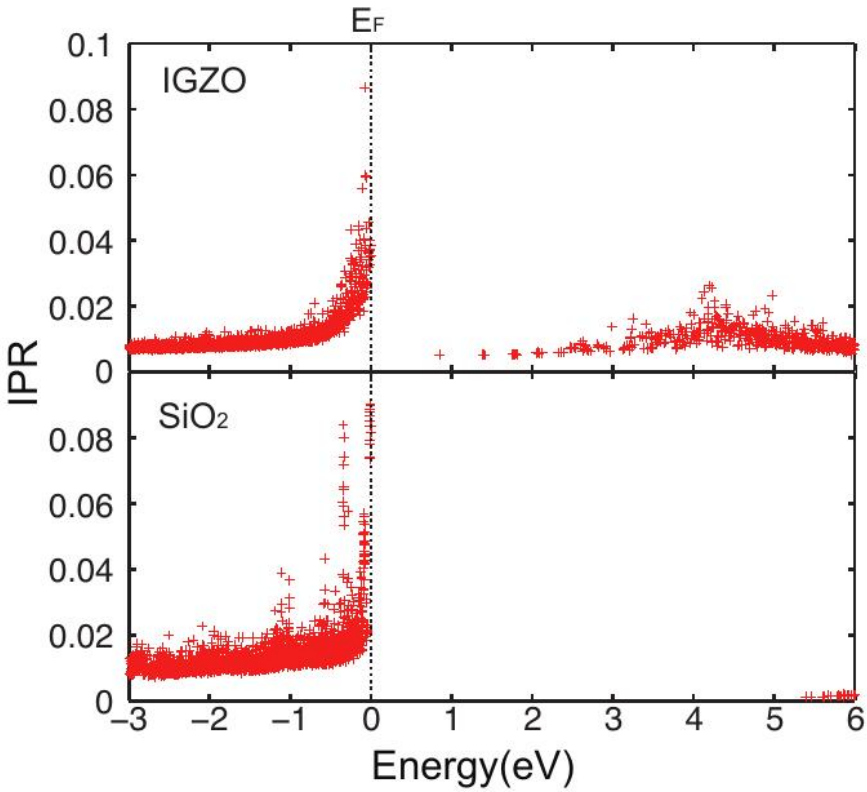

Figure 4.6. Inverse-participation ratios value of *a*-IGZO and *a*-SiO_2, respectively

4.6. Band alignment

To calculate valence band offset between hetero junction we used a formula in the below:[40]

$$E_{\mathrm{VBO}} = (E_{\mathrm{VBO}} - E^{ref})_{\mathrm{IGZO}} - (E_{\mathrm{VBO}} - E^{ref})_{\mathrm{SiO_2}} + \triangle E^{ref} \ , \qquad (7)$$

where E_{VBM} represents the top of valence band of *a*-IGZO and *a*-SiO_2, respectively, calculated within the bulk structures. E^{ref} is a selected reference energy that converge fast with respect to the number of layers in interface model. And, $\triangle E^{\mathrm{ref}}$ is the difference between reference energy of each of bulk-like region in the interface calculation. In general, various quantities can be used as reference energy, like atomic core levels or plane averaged electrostatic potential. But amorphous structures have no symmetry, atomic core levels and averaged electrostatic potential are notably scattered and it is hard to define reference level from bulk and interface model neither.

In this work, the energy level of oxygen 2*s* level was used to align the

valence band maxima. To calculate oxygen 2*s* level, we used first moment of partial density of states for O 2*s*::

$$E_{2s}^{i} = \frac{\int_{-\infty}^{E_F} (\epsilon - E_F) D_{2s}^{i}(\epsilon) d\epsilon}{\int_{-\infty}^{E_F} D_{2s}^{i}(\epsilon) d\epsilon} \tag{8}$$

where $D_{2s}^{i}(\epsilon)$ is partial density states of 2*s* orbital of *i* th oxygen.
As the first moment value are dispersive among the atoms, we need to average the first moment along z-axis.

$$\overline{E_{2s}}(z) = \frac{1}{2\lambda} \int_{z-\lambda}^{z+\lambda} z \int_{0}^{L_x} dx \int_{0}^{L_y} dy \sum_{i}^{O_{xy}} \delta(\boldsymbol{r} - \boldsymbol{r_i}) \tag{9}$$

Figure 4.7. illustrates the result of above formula averaged over 6 different interface model, which is constructed by same amorphous structures. As you can see in the figure, oxygen 2*s* level shows about

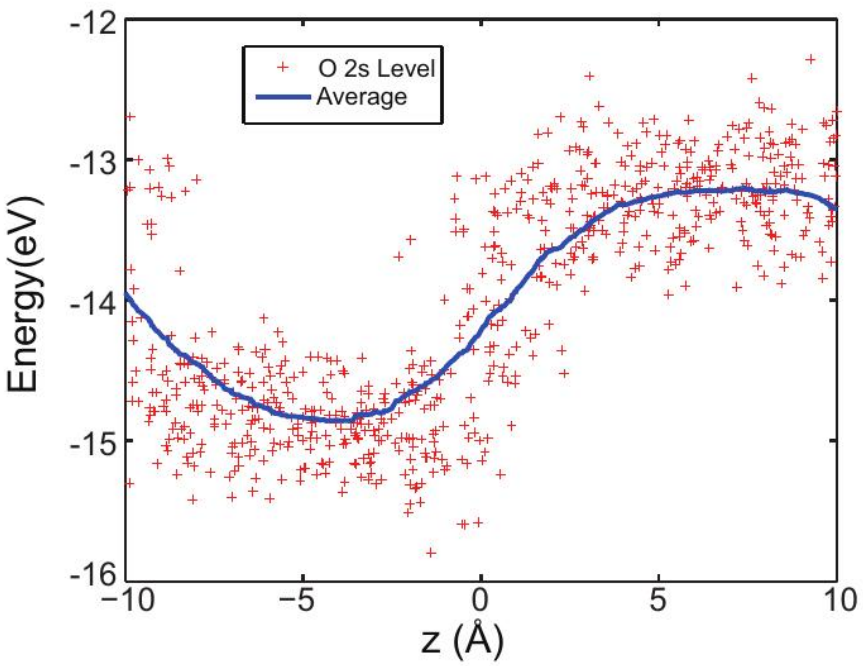

Figure 4.7. Oxygen 2*s* level chosen as reference level (red dots), and averaged line (blue line).

1.6 eV difference between two bulk regions.

The band offset was represented in Fig. 4.8. including gap correction by HSE06 calculation. The valence band offset is obtained from GGA and conduction band correction is done with HSE06 data. The valence band offset values is 1.43 eV. [41] In the experiment, they measure the delocalized-to-delocalized transition gap, the value 1.43 eV corresponds to 1.0 eV in our calculation. It show a reasonable agreement.

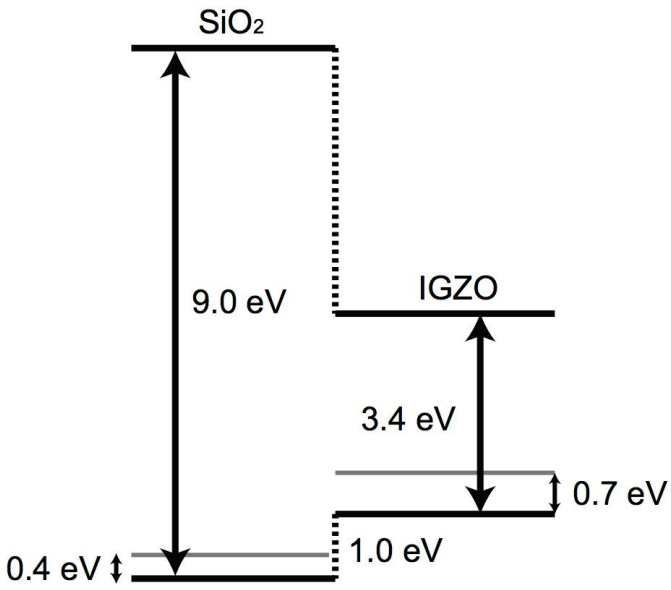

Figure 4.8. Band offset calculated from GGA of interface between *a*-SiO2/*a*-IGZO. Gray lines represent locaized tail state edges.

4.7. Partial density of states

Partial density of states is represented in Fig. 4.9. In interface calculations, we separated partial density of state as 3 parts, *a*-IGZO-bulk-like region, *a*-SiO2-bulk-like region, and interface region. The figure was from GGA+U calculation, so energy gap of system is much underestimated than experiment.

Compare to DOS of real bulk systems, DOS of *a*-IGZO-bulk-like region and *a*-SiO_2-bulk-like region in the interface shows great correspondence. The top of valence band of total interface system is in *a*-$IGZO_4$-bulk-like region and the bottom of valence band is too. Hence, band gap of total system is determined to be that of *a*-IGZO.

The figure was obtained from an energetically favorable interface model, in that cases there is no subgap state formed at the interface. This is because that two materials forming interfaces have similar characteristic valence band which are both major contribution is made up of oxygen *p* orbital, which make character of valence band of interface region similar with bulk region. And both materials are amorphous structures, it is easy to relax electronically unfavorable bonds. One more interesting point is that valance band offset (which includes tail states) in partial DOS and LDOS (Fig. 4.11.) gives 1.3 eV.

It corresponds to the value of previous approach, which is reference level approach.

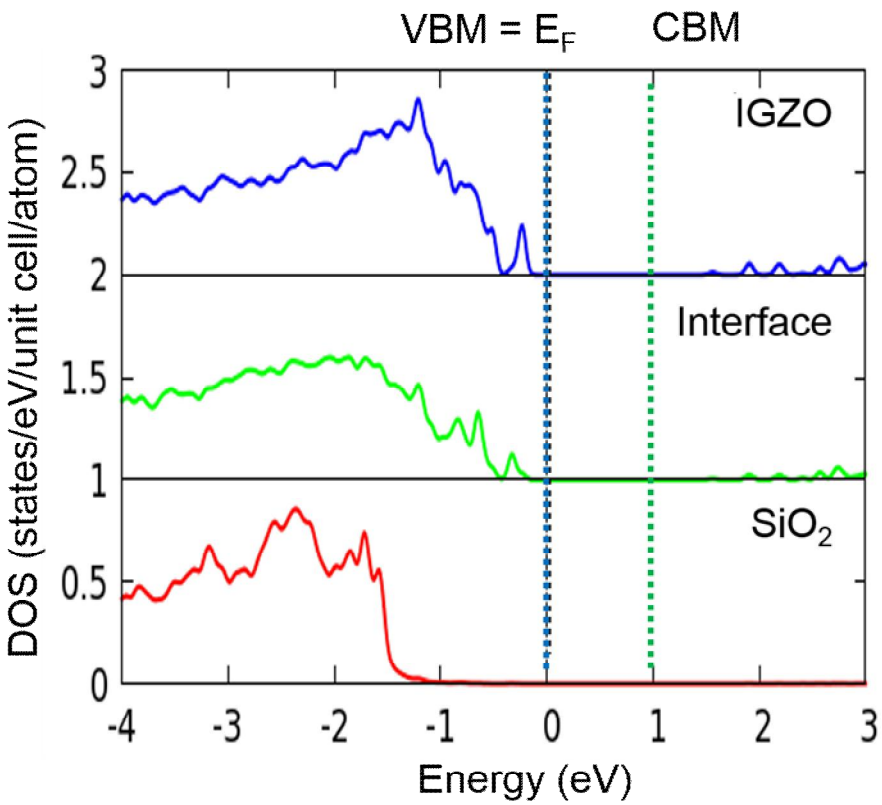

Figure 4.9 Partial DOS of *a*-IGZO-bulk-like region, interface region and *a*-SiO_2 bulk-like region

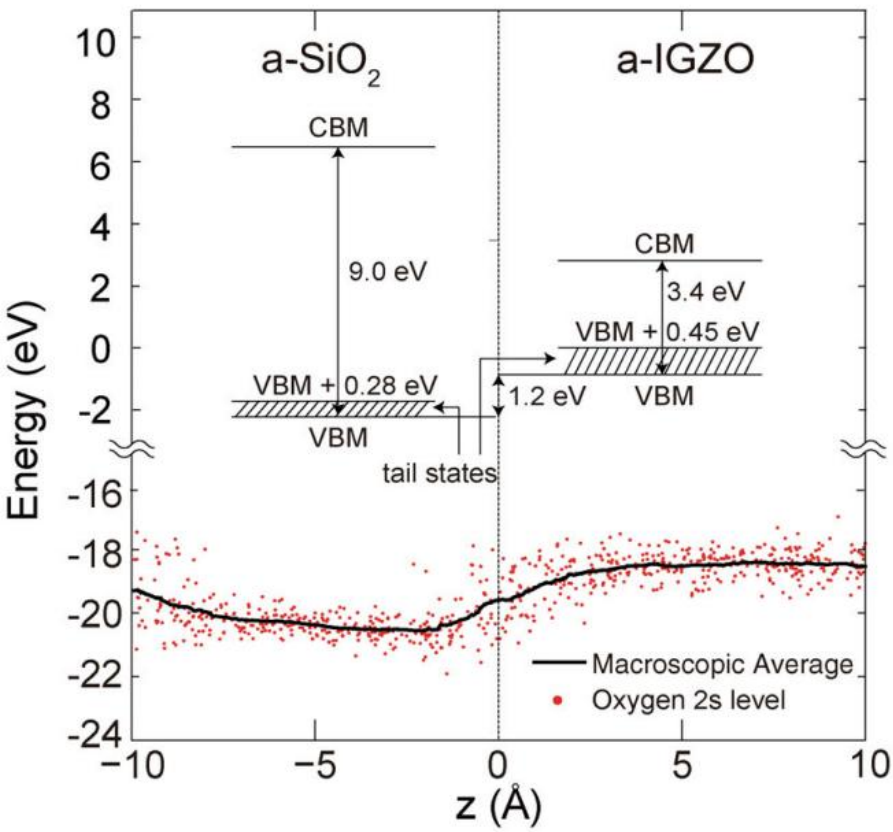

Figure 4.10 The schematic diagram for the electronic structure of the constructed interface is shown. The calculated first-moment peaks for oxygen 2s level are plotted. The plateaus in the macroscopic average indicate the bulk regions of a-SiO_2 and a-IGZO.

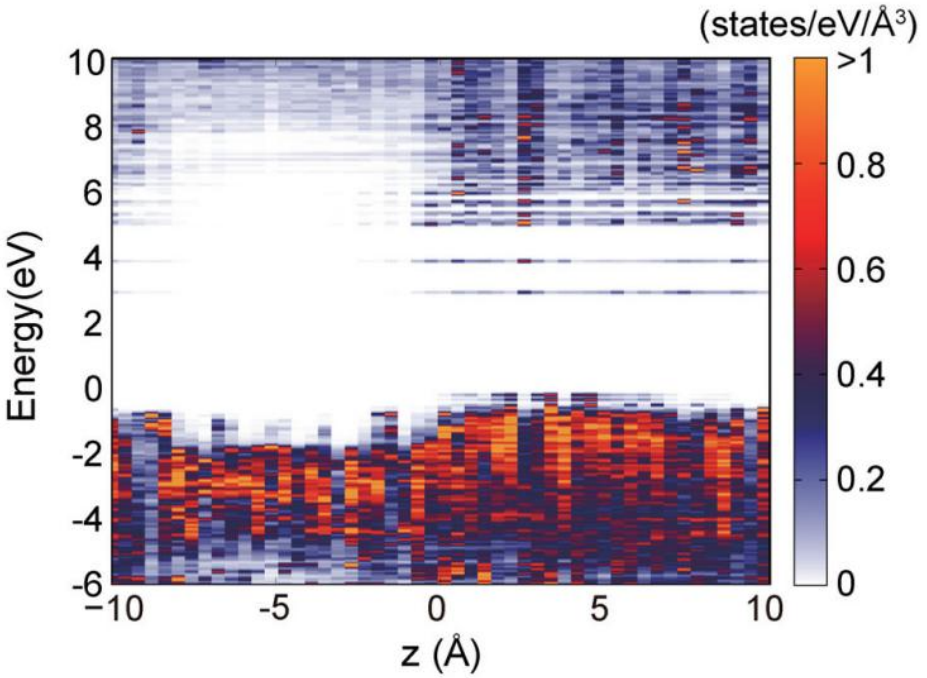

Figure 4.11 Calculated partial density of states that is spatially resolved along the z-direction.

4.8. V_O at the interface

We introduce one V_O by removing an oxygen atom from the interface models, and fully relax the atomic positions within GGA + U functional. For the statistical average, two interface models are selected and about 180 V_O configurations are studied. We first compute the formation energy of the neutral V_O:

$$\Omega_V = E_{tot}(V_O) - E_{tot}(\text{interface}) + \mu_O,$$

where $E_{tot}(V_O)$ is total energy of the interface model including V_O, and μ_O is the oxygen chemical potential. Here, μ_O is set to the half of the total energy of the oxygen molecule, corresponding to the oxygen-rich condition.

It has been well established that the formation energy of the shallow defect levels in semiconducting oxides suffers from the error caused by the band-gap underestimation and large dispersion in the conduction

bands. In order to reduce errors in Ω_V for the shallow defect state, we first determine the nature of each defect by examining its band dispersion and spatial distribution. For the oxygen vacancy concluded to be shallow in nature, we correct Ω_V by adding the band-gap error in GGA + U results.

Figure 4.12. shows the calculated Ω_V with respect to the z-position of V_O. The V_O's can be classified into four types according to the neighboring cations and deep/shallow characters: (i) deep V_O with Si-Si bond (V_O[Si-Si]), (ii) deep V_O with metal-metal bond (V_O[M-M]; M = In, Ga, or Zn) or (iii) shallow V_O with the broken metal bond (V_O[M · · · M]), and (iv) deep V_O with metal-Si bond (V_O[M-Si]).

In Fig. 4.12., it is noteworthy that the deep levels are formed for many V_O's at the interface and they are accompanied by the metal-Si bonds. Figure 4.13. (a) shows the detailed atomic configuration and local density of states. A dashed circle in Fig. 4.13. (a) confirms that the localized defect level is developed at the interface. As shown in the right figure, it is found that most of this state (more than 70%) is distributed over Si, metal, and surrounding oxygen atoms. Since two electrons occupy this state, the interfacial V_O can play as hole-trapping sites.

The hole trapping into the deep interfacial V_O can be mimicked by removing two electrons from the supercell. Figure 4.13. (b) shows the relaxed geometry and the corresponding electronic structure for V^{2+}_O [M -Si]. It is noticeable that the bond length of $[M \cdot \cdot \cdot Si]^{2+}$ is significantly elongated from 2.45 to 4.24 Å. Concurrently, the localized

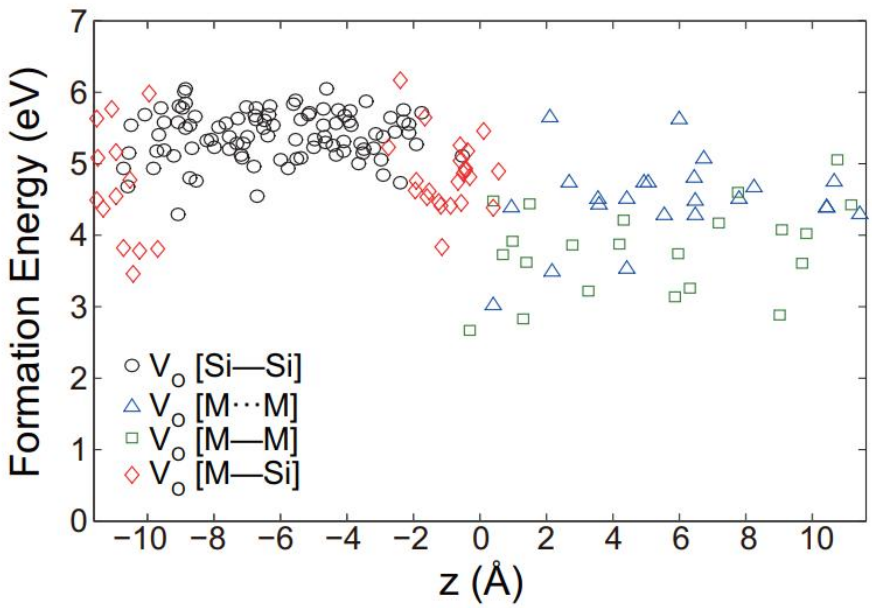

Figure 4.12 The formation energy of the neutral oxygen vacancy is shown with respect to the z-coordination. The vacancies are classified into four types according to neighboring cations.

level with the band gap shifts into the conduction band and becomes a resonant

state. We find that most interfacial V_O[M-Si]' s undergo similar deep-to-resonant transition upon hole trapping.

Based on the above V_O[M-Si], we propose a microscopic mechanism of the NBIS instability. First, the interfacial V_O[M-Si] could be generated during the growth process. Although V_O[M-Si] is less stable than V_O in a-IGZO bulk on average (see Fig. 3), the non-equilibrium condition may allow for the substantial generation of V_O[M-Si]. Furthermore,

under the NBIS condition, ionized V^{2+}_O can electro-migrate and accumulate at the interface. At the same time, the photo-excited holes in the channel layer will drift to the interface between the a-IGZO channel and a-SiO_2. Then, the holes will be captured by V_O[M-Si], followed by the deep-to-resonant transition from V_O[M-Si] to V^{2+}_O [M・・・Si]. When NBIS is off, the captured holes would recombine with electrons if the energy barrier from Fig. 12 (b) to Fig. 12 (a) is overcome by thermal fluctuation. Even though we were not able to calculate the recovery barrier since the transition path is too complex, the large structural change in V^{2+}_O [M・・・Si] strongly suggests that the barrier should be significantly higher than for V^{2+}_O in the bulk region of a-IGZO. Therefore, we suggest that the V_O[M-Si] at the interface can contribute to the long-term negative shift of V_{th} in TFTs.

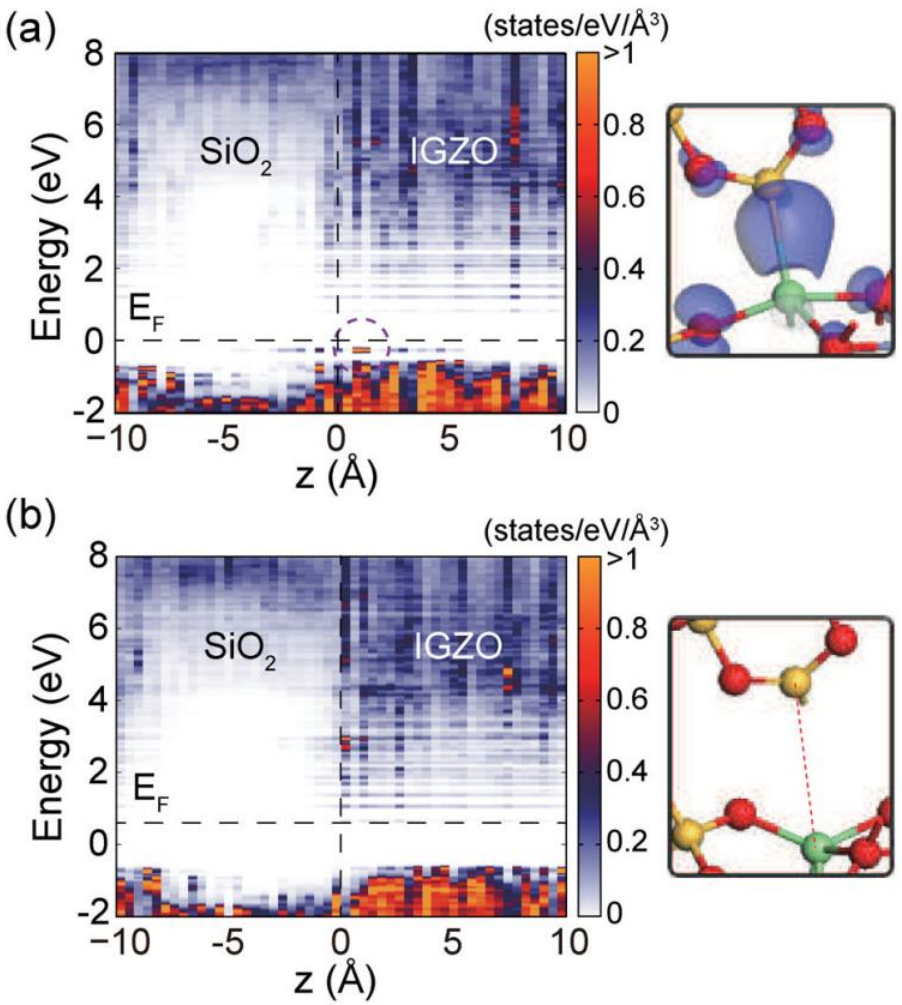

Figure 4.13 The local densities of states and atomic structures of (a) deep V_O[M−Si] and (b) resonant V_O[M···Si] are shown. The isosurface of the charge density of the defect state marked by the dashed circle in (a) is shown in the right. The isovalue is 3.4×10−3 e $Å^{-3}$

CHAPTER 5

Conclusion

In this paper, we investigated the nature of V_O in a-IGZO bulk and interface between channel/dielectric layers using first-principles calculations. In the bulk, to circumvent the two modeling issues associated with the band gap and vacancy configuration, the hybrid density functional MD simulations were employed to generate oxygen deficient amorphous models. Our analysis on the electronic structure and energetics of V_O models showed that the majority of oxygen vacancies acts as shallow donors in a-IGZO. In addition, the interface structure was modeled by carefully joining the two amorphous phases such that interface bonds between oxygen and Si/metal atoms were fully formed. The band offset was computed by aligning the oxygen 2s level and shows good agreement with experiment. For the stoichiometric interface, we could not find any charge trap levels within the band gap. This suggests that the clean interface without charge trapping sites can be synthesized in experiment. On the other hand, when V_O was introduced at the interface, the Si-metal bonds were formed together with the deep defect levels (V_O[M-Si]). We simulated the hole trapping into this defect by removing two electrons and it was found that the local structure near the Si-metal bond undergo a large relaxation. This implies that the recovery to the original neutral state would involve a large energy barrier. We believe that this is one of

the main origin of the long-term stability issue in a-IGZO-based TFTs. The present results are also consistent with the recent experiment demonstrating the improvement in NBIS stability when the thermal annealing reduced the density of interfacial V_O.

Bibliography

[1] K. Nomura, H. Ohta, A. Takagi, T. Kamiya, M. Hirano and H. Hosono, Nature 432, 488 (2004).

[2] K. Nomura, H. Ohta, K. Ueda, T. Kamiya, M. Hirano and H. Hosono, Science 300, 1269 (2003).

[3] M. W. J. Prins, K.-O. Grosse-Holz, G. Müller, J. F. M. Cillessen, J. B. Giesbers, R. P. Weening and R. M. Wolf, Appl. Phys. Lett. 68, 3650 (1996).

[4] M. W. J. Prins, S. E. Zinnemers, J. F. M. Cillessen and J. B. Giesbers, Appl. Phys. Lett. 70, 458 (1997).

[5] R. L. Hoffman, B. J. Norris and J. F. Wager, Appl. Phys. Lett. 82, 733 (2003).

[6] P. F. Carcia, R. S. McLean, M. H. Reilly, and G. Nunes Jr., Appl. Phys. Lett. 82, 1117 (2003).

[7] R. L. Hoffman, Journal of Applied Physics 95, 5813 (2004).

[8] D. H. Lee, K.-I. Kawamura, K. Nomura, T. Kamiya and H. Hosono, Electrochem. Solid-State Lett. 13, H324 (2010).

[9] D. H. Lee, K.-I. Kawamura, K. Nomura, H. Yanagi, T. Kamiya, M. Hirano and H. Hosono, Thin Solid Films 518, 3000 (2010).

[10] S. Jeon, S.-E. Ahn, I. Song, C. J. Kim, U-I. Chung, E. Lee, I. Yoo, A. Nathan, S. Lee, K. Ghaffarzadeh, J. Robertson and K. Kim, Nat. Mater. 11, 301 (2012).

[11] E. Na. Cho, J. H. Kang, C. E. Kim, P. Moon and I. Yun, IEEE Trans. Device Mater. Rel. 11, 112 (2011).

[12] M. D. H. Chowdhury, P. Migliorato and J. Jang, Appl. Phys. Lett. 98, 153511 (2011)

[13] H. Oh, S. Yoon, M. Ryu, C. Hwang, S. Yang and S. Park, Appl. Phys. Lett. 97, 183502 (2010)

[14] H.-K. Noh, K. J. Chang, B. Ryu, and W.-J. Lee, Phys. Rev. B 84, 115205 (2011).

[15] B. Ryu, H.K. Noh, E.A. Choi, and K.J. Chang, Appl. Phys. Lett. 97, 022108 (2010).

[16] H. Li, Y. Guo, and J. Robertson, Phys. Rev. Mater. 2, 074601 (2018).

[17] T. Kamiya, K. Nomura, M. Hirano, and H. Hosono, Phys. Status Solidi C 5, 3098 (2008).

[18] A. de Jamblinne de Meux, A. Bhoolokam, G. Pour- tois, J. Genoe, and P. Heremans, Phys. Status Solidi A 214, 1600889 (2017).

[19] I. J. Kang and C. Park, arXiv preprint arXiv:1108.2086 (2011).

[20] T. Kamiya, K. Nomura, and H. Hosono, Phys. Status Solidi A 206, 860 (2009).

[21] T. Kamiya, K. Nomura, and H. Hosono, Phys. Status Solidi A 207, 1698 (2010).

[22] P. Hohenberg and W. Kohn, Phys. Rev. 136, B864 (1964).

[23] W. Kohn and L. Sham, J. Phys. Rev. 140, A1133 (1965).

[24] J. P. Perdew and W. Yue, Phys. Rev. B 33, 8800 (1986).

[25] A. D. Becke, Phys. Rev. A 38, 3098 (1988).

[26] J. P. Perdew, M. Emzerhog and K. Burke, Phys. Rev. Lett. 77, 3865 (1996).

[27] A. I. Liechtenstein, V. I. Anisimov and J. Zaane, Phys. Rev. B 52, R5467 (1995).

[28] J. Heyd, G. E. Scuseria and M. Ernzerhof, J. Chem. Phys. 118, 8207-8215 (2003).

[29] A. V. Krukau, O. A. Vydrov, A. F. Izmaylov and G. E. Scuseriaa J. Chem. Phys. 125, 224106 (2006).

[30] F. Evers and A. D. Mirlin, Phys. Rev. Lett. 84, 3690 (2000).

[31] T. Kamiya, K. Nomura, and H. Hosono, J. Disp. Technol. 5, 468 (2009).

[32] W.-J. Yin, J. Ma, S.-H. Wei, M. M. Al-Jassim, and Y. Yan, Phys. Rev. B 86, 045211 (2012).

[33] Y. Kang, H. Song, H. H. Nahm, S. H. Jeon, Y. Cho, and S. Han, APL Mater. 2, 032108 (2014).

[34] D.Y. Cho, J. Song, K.D. Na, C.S. Hwang, J.H. Jeong, J. K. Jeong, and Y. G. Mo, Appl. Phys. Lett. 94, 112112 (2009).

[35] G. Kresse, and J. Furthmuller, Phys. Rev. B 54, 11189 (1996).

[36] P. E. Blöchl, Phys. Rev. B 50, 17953 (1994).

[37] N. J. Mosey, P. Liao, E. A. Carter, J. Chem. Phys. 129, 014103 (2008).

[38] J. Hartford, Phys. Rev. B 61, 2221 (2000).

[39] X. Zhang, A. A. Demkov, Hao Li, X. Hu, and Yi Wei, J. Kulik, Phys. Rev. B 68, 125323 (2003).

[40] E. Flage–Larsen* and O. M. Løvvik, C. M. Fang and G. Kresse, Phys. Rev. B 88, 165310 (2013).

[41] E. A. Douglas, A. Scheurmann, R. P. Davies, B. P. Gila, H. Cho, V. Craciun, E. S. Lambers, S. J. Pearton, and F. Ren, Appl. Phys. Lett. 98, 242110 (2011).

[42] T. Kamiya and H. Hosono, NPG Asia Mater. 2, 15 (2010).

[43] T. Kamiya, K. Nomura, and H. Hosono, Sci. Technol. Adv. Mater. 11, 044305 (2010).

[44] H. Y. Jung, Y. Kang, A. Y. Hwang, C. K. Lee, S. Han, D.-H. Kim, J.-U. Bae, W.-S. Shin, and J. K. Jeong, Sci. Rep. 4, 3765 (2014).

[45] H.-H. Nahm, Y.-S. Kim, and D. H. Kim, Phys. Status Solidi B 249, 1277 (2012).

[46] M. D. H. Chowdhury, P. Migliorato, and J. Jang, Appl. Phys. Lett. 97, 173506 (2010).

[47] K. H. Ji, J.-I. Kim, H. Y. Jung, S. Y. Park, R. Choi, U. K. Kim, C. S. Hwang, D. Lee, H. Hwang, and J. K. Jeong, Appl. Phys. Lett. 98, 103509 (2011).

[48] J. K. Jeong, H. W. Yang, J. H. Jeong, Y.-G. Mo, and H. D. Kim, Appl. Phys. Lett. 93, 123508 (2008).

[49] K. Nomura, T. Kamiya, and H. Hosono, Appl. Phys. Lett. 99, 053505 (2011).

[50] J. Robertson and Y. Guo, Appl. Phys. Lett. 104, 162102 (2014).

[51] J.-Y. Kwon, J. S. Jung, K. S. Son, K.-H. Lee, J. S. Park, T. S. Kim, J.-S. Park, R. Choi, J. K. Jeong, B. Koo, and S. Y. Lee, Appl. Phys. Lett. 97, 183503 (2010).

[52] M. D. H. Chowdhury, J. G. Um, and J. Jang, Appl. Phys. Lett. 105, 233504 (2014).

[53] H. Oh, S.-M. Yoon, M. K. Ryu, C.-S. Hwang, S. Yang, and S.-H. K. Park, Appl. Phys. Lett. 98, 033504 (2011).

[54] P. Broqvist, A. Alkauskas, J. Godet, and A. Pasquarello, J. Appl. Phys. 105, 061603 (2009).

[55] G. Kresse and J. Hafner, Phys. Rev. B 47, 558 (1993).

[56] J. P. Perdew, A. Ruzsinszky, G. I. Csonka, O. A. Vydrov, G. E. Scuseria, L. A. Constantin, X. Zhou, and K. Burke, Phys. Rev. Lett. 100, 136406 (2008).

[57] S.L.Dudarev, G.A.Botton, S.Y.Savrasov, C.J.Humphreys, and A. P. Sutton, Phys. Rev. B 57, 1505 (1998).

[58] K. Nomura, T. Kamiya, E. Ikenaga, H. Yanagi, K. Kobayashi, and H. Hosono, J. Appl. Phys. 109, 073726 (2011).

[59] A. Hino, S. Kosaka, S. Morita, S. Yasuno, T. Kishi, K. Hayashi, and T. Kugimiya, ECS Solid State Lett. 1, Q51(2012).

[60] A. Pasquarello and R. Car, Phys. Rev. Lett. 79, 1766 (1997).

[61] Y. J. Oh, H.-K. Noh, and K. J. Chang, Physica B 407, 2989 (2012).

[62] Y. Tu and J. Tersoff, Phys. Rev. Lett. 84, 4393 (2000).

[63] W.-J. Son, E. Cho, B. Lee, J. Lee, and S. Han, Phys. Rev. B 79, 245411 (2009).

[64] Y. Jeong, C. Bae, D. Kim, K. Song, K. Woo, H. Shin, G. Cao, and J. Moon, Appl. Mater. Interfaces 2, 611 (2011).

[65] Y.-G. Lee and W.-S. Choi, Electron. Mater. Lett. 9, 719 (2013).

[66] T. Tamura, G.-H. Lu, and R. Yamamoto, Phys. Rev. B 69, 195204 (2004).

[67] H. Kumomi, K. Nomura, T. Kamiya, and H. Hosono, Thin Solid Films 516, 1516 (2008).

[68] J. Sheng, H. J. Jeong, K. L. Han, T. Hong, and J. S. Park, J. Inf. Disp. 18, 159 (2017).

국문초록

투명 산화물 반도체는 비정질 구조임에도 불구하고 높은 전자 이동도를 보여준다. 게다가 비정질 구조 덕분에 균질도가 높아 대면적으로 만들기 유리하고, 투명한 성질을 가진다. 때문에 투명 산화물 반도체는 차세대 디스플레이 기기에서 핵심적인 역할을 하게 될 가능성이 높다. 하지만 신뢰성 문제가 투명 산화물 반도체의 발전에 치명적인 약점으로 작용한다. 특히 심각한 것은 빛과 관련한 불안정성이다. 이러한 빛에 의한 불안정성의 원인으로는 산소 공공과 반도체/유전체 사이의 계면이 지목되곤 했다.

산소 공공의 경우 밀도범함수이론 (density functional theory, DFT)을 이용한 여러 연구들이 진행되었지만, 여러 연구들이 서로 상충되는 결과들을 보고했다. 주로 논란이 되는 부분은 산소 공공이 deep donor 로 작용하느냐 아니면 shallow donor 의 성격을 띄느냐 하는 부분이다. 이 연구에서는 이전의 연구들이 고려하지 않았던 새로운 계산 방법들을 적용하여 보다 정확도 높은 밀도범함수이론 연구를 하고자 했다. 첫 번째는 산소 공공을 만드는 전과정에서 HSE06을 이용하여 band gap correction을 진행했고, 두 번째는 처음부터 산소가 부족한 cell을 melt-quench하여 결함구조를 생성하였다. 8개의 산소가 부족한 모델을 생성하였고, 모두가 shallow donor를 생성함을 확인하였다. 또한 두 개의 전자를 더 투입하여 melt-quench 과정을 거치게 한 8개의 모델 중 5개가 deep donor를 생성함을 확인 하였다. 그렇게 만든 deep donor 모델과 shallow

donor 모델들을 전하가 중립인 상태에서의 에너지 비교를 진행했고, 평균적으로 shallow donor 모델들이 더 안정한 것으로 계산되었다.

또한, Negative 전압과 빛이 함께 가해진 상황 (negative-bias-illumination stress, NBIS)에서 발생하는 구동전압 변화가 비정질 산화물 반도체와 유전체 사이의 계면의 특성에 의해 결정된다는 주장이 제기된 바 있다. 하지만 비정질 구조 사이의 계면의 특성상 그 동안 해당 계면에 대한 밀도범함수이론 연구는 진행된 바가 없었다. 이 연구에서는 비정질 산화물 반도체와 비정질 유전체 사이의 계면을 MD 시뮬레이션을 통해 모델링하여 밴드 정렬 값을 통해 시뮬레이션의 정확도를 확인하였고, 에너지적으로 안정한 구조에서는 hole trap이 될 만한 구조가 생성되지 않음을 확인했다. 또한 계면에서 산소 공공이 발생할 경우 metal silicate 결합이 발생되면서 hole trap이 될 수 있음을 밝혔다.

주요어 : 밀도범함수이론, 비정질 산화물 반도체, 산소 공공, 비정질 계면, hole trap site

학 번 : 2014-30224